

# Linear stability of the boundary layer under a solitary wave

Joris C. G. Verschaeve<sup>1\*</sup> & Geir K. Pedersen<sup>2</sup>

<sup>1</sup>Norwegian Geotechnical Institute, Po.Box 3930, Ullevål Stadion,  
0806 Oslo, Norway

<sup>2</sup>University of Oslo, Po.Box 1072 Blindern, 0316 Oslo, Norway

February 27, 2024

## Abstract

A theoretical and numerical analysis of the linear stability of the boundary layer flow under a solitary wave is presented. In the present work, the nonlinear boundary layer equations are solved. The result is compared to the linear boundary layer solution in Liu et al. (2007) revealing that both profiles are disagreeing more than has been found before. A change of frame of reference has been used to allow for a classical linear stability analysis without the need to redefine the notion of stability for this otherwise unsteady flow. For the linear stability the Orr-Sommerfeld equation and the parabolic stability equation were used. The results are compared to key results of inviscid stability theory and validated by means of a direct numerical simulation using a Legendre-Galerkin spectral element Navier-Stokes solver. Special care has been taken to ensure that the numerical results are valid. Linear stability predicts that the boundary layer flow is unstable for the entire parameter range considered, confirming qualitatively the results by Blondeaux et al. (2012). As a result of this analysis the stability of this flow cannot be described by a critical Reynolds number unlike what is attempted in previous publications. This apparent contradiction can be resolved by looking at the amplification factor responsible for the amplification of the perturbation. For lower Reynolds numbers, the boundary layer flow becomes unstable in the deceleration region of the flow. For higher Reynolds numbers, instability arises also in the acceleration region of the flow, confirming, albeit only qualitatively, an observation in the experiments by Sumer et al. (2010).

---

\*Email address for correspondence: joris@math.uio.no

# 1 Introduction

Solitary waves are frequently encountered in experimental and theoretical fluid mechanics. This is not only due to the existence of approximate solutions for solitary waves, see for instance Grimshaw (1971) or Fenton (1972), but also a consequence of the fact that solitary waves are relatively simple to generate under laboratory conditions with good reproducibility. Solitary waves display a series of remarkable properties, cf Miles (1980). The key feature herein is the preservation of their shape during propagation. This is, however, only true in the limit of vanishing frictional effects by the air and the bottom. In reality, due to nonzero viscosity a thin boundary layer will develop between water and air and between water and bottom. These boundary layers will lead to a drain of energy finally dissipating the solitary wave Shuto (1976); Miles (1980). Although very small for solitary waves on relatively large depths, such frictional effects become more important for cases where the layer of water becomes thin. This can be the case for solitary waves on small depths or when the solitary wave is running up a beach which leads to a large discrepancy between theoretical and experimental run up heights Pedersen et al. (2013).

The bottom boundary layer has been considered to be the more relevant, cf. Liu and Orfila (2004), and research has focused on it. Investigation of the bottom boundary layer under a solitary wave has been initiated by Liu et al. (2007) when they published theoretical and experimental results concerning the shape of the boundary layer profile. This work has led to subsequent publications by Sumer et al. (2010), Vittori and Blondeaux (2008, 2011) and Blondeaux et al. (2012) investigating the transitions in the boundary layer. Sumer et al. (2010) investigated experimentally the stability of the boundary layer flow under a solitary wave, Vittori and Blondeaux (2008, 2011) performed direct numerical simulations to this end and Blondeaux et al. (2012) were the first to perform a linear stability analysis on this type of flow. A result of the works by Sumer et al. (2010) and Vittori and Blondeaux (2011) is that the regimes of the boundary layer flow can be categorized into three to four regimes Sumer et al. (2010): laminar, laminar with regular vortex tubes, transitional and fully turbulent. The transition between the first and the second regime is predicted by Vittori and Blondeaux (2008) to happen at a Reynolds number  $Re_{\text{Sumer}}$  somewhat below  $Re_{\text{Sumer}} = 5 \times 10^5$ , whereas Sumer et al. (2010) measured it to be lower, namely at  $Re_{\text{Sumer}} = 2 \times 10^5$ . Here  $Re_{\text{Sumer}}$  is a Reynolds number defined by Sumer et al. (2010) which is based on particle displacement and maximum velocity in the outer flow as length and velocity scale, respectively. Vittori and Blondeaux (2011) proposed that circumstantial laboratory conditions, such as wall roughness or vibrations, perturbed the system and led to a lowering of the critical Reynolds number. As Blondeaux et al. (2012) concluded later, the flow under a solitary wave is always unstable in the sense of linear stability and they suggested to use the growth of the kinetic energy attached to the perturbations as a measure for the appearance of transitions in the flow. However, a linear stability analysis as presented in Blondeaux et al. (2012) cannot predict whether the flow after transition is turbulent or not, contrary to what the title of Blondeaux et al.

(2012) suggests. In a recent study Pedersen et al. (2013) measured boundary layers during runup of solitary waves on a beach. They observed instabilities (undulations and vortices) for Reynolds numbers which were higher than those of Sumer et al. (2010), when defined in a corresponding manner. However, the runup flow is different from that under a solitary wave on constant depth, due to the moving shoreline and the relatively longer retardation phase as compared to the acceleration phase, which makes direct comparison difficult.

In spite of the progress made in the aforementioned references, a number of issues remain and need to be addressed. The outer velocity field in Sumer et al. (2010), Vittori and Blondeaux (2008, 2011) and Blondeaux et al. (2012) was either given by the simple secant hyperbolic formula Miles (1980) or the third order approximate formula by Grimshaw (1971). Both velocity fields deviate markedly from the true velocity field. In addition, for the experiments in Sumer et al. (2010), and the numerical simulations in Vittori and Blondeaux (2008, 2011) and Blondeaux et al. (2012), the outer velocity field was made 'spatially uniform'. A result of the process of uniformization is that nonlinear terms of the boundary layer equations are neglected and the wall normal velocity component is put to zero. This results in a different boundary layer flow, thereby excluding nonlinear and nonparallel effects. A justification for this uniformization was founded on the conclusion by Liu et al. (2007), that the linear boundary layer flow approximates the nonlinear one very closely. This conclusion is, however, based on an erroneous formula given in Liu and Orfila (2004) and therefore not properly justified. In addition, a common difficulty encountered in the works by Sumer et al. (2010), Vittori and Blondeaux (2008, 2011) and Blondeaux et al. (2012) is that the flow of a solitary wave is time dependent and therefore the notion of hydrodynamic stability needed to be redefined. However, the risk is then that the resulting definition is of descriptive nature, rather than being mathematically concise, as for example in Sumer et al. (2010) and Vittori and Blondeaux (2008, 2011), where instability simply meant that something unexpected became visible. The relation between local instabilities, either temporal or spatial, to a global instability of a non-uniform flow may in general be complex (see, for instance Huerre and Monkewitz, 1990) and the application of approximate stability analysis, such as one involving a uniform flow assumption, must be carefully checked. Blondeaux et al. (2012) justify their application of the Orr-Sommerfeld equation for the transient flow under a solitary wave by assuming that the growth of instabilities takes place on a time scale much faster than the time scale of the basic flow. However, this assumption is incorrect, at least close to neutral stability. On the other hand, as will be shown subsequently, through comparison with more general theories, their version of the Orr-Sommerfeld equation still performs reasonably well. Another issue, which is not sufficiently elaborated in the references, is the seeding, or triggering, of the perturbation in the flow. Vittori and Blondeaux (2008, 2011) applied white noise with an amplitude of  $10^{-4}$  as a seeding for the perturbation before the arrival of the solitary wave. Sumer et al. (2010) did not introduce any perturbation in their experiments at all, but relied instead on a natural seeding by the experimental environment. In general neither the frequency nor the amplitude

of the perturbation have been controlled in Vittori and Blondeaux (2008, 2011) and Sumer et al. (2010).

In the present treatise, the incorrect formulae in Liu et al. (2007) are discussed and the corrected nonlinear boundary layer solution is presented. To avoid dealing with a transient boundary value problem, a simple change of frame of reference is made. In the frame of reference of the solitary wave, the boundary layer flow is stationary and the entire range of classical theory of hydrodynamic stability Drazin and Reid (1981) can be applied. The stability properties of the viscous boundary layer under a solitary wave are thus obtained using classical methods of linear stability theory. In particular the Orr-Sommerfeld equation Drazin and Reid (1981) and the parabolic stability equation Bertolotti et al. (1992) were used to find the unstable regions of the boundary layer flow. For this type of flow, the criterion of amplification Jordinson (1970); Bertolotti et al. (1992) can be used to characterize the flow. The results by means of this amplification criterion indicate that the transition in the boundary layer flow under a solitary wave might neither be characterized by a critical Reynolds number  $Re_{\text{Sumer}}$  Sumer et al. (2010); Vittori and Blondeaux (2011) nor by a critical set of parameters  $(\delta_c, \epsilon_c)$  Vittori and Blondeaux (2008); Blondeaux et al. (2012). Instead, the mere appearance of vortex tubes, say, will depend in a large amount on the initial amplitude of the perturbation. In addition, as was observed by Sumer et al. (2010) for higher Reynolds numbers, the transition is characterized by a growth of perturbations in the acceleration region of the boundary layer, i.e. where the pressure gradient favors stability. This can be explained by the development of a 'viscous' instability, akin to that for the Blasius profile, as shown by linear stability in the present treatise. A direct numerical simulation by means of a Navier-Stokes solver was performed to verify the results obtained by linear stability analysis.

The present discussion is organized as follows. The physical problem and the equations treated in the present discussion are briefly explained in section 2. The numerical schemes used to solve the equations are presented in section 3. Section 4 presents results and discussion of the present investigation. A short summary and the final conclusions are given in section 5.

Since the present work is based on a numerical analysis using different techniques we decided to give a short description of the numerical methods used in section 3. Verification and validation are important for all numerical applications, but should be particularly indispensable for stability models. Still, in the literature these aspects are often superficially treated and the trustworthiness of the numerical results cannot be properly assessed. Hence, the schemes are concisely outlined in section 3, while benchmarking is left for the appendices A- D. This should enable the reader to make an independent judgment of the strengths and limitations of the present numerical analysis. Readers mainly interested in the physical content, on the other hand, might skip section 3, and go directly to the results in section 4.

## 2 Description of the problem

Herein, we investigate a solitary wave with amplitude  $\epsilon h_0$  propagating from right to left on a flat bottom at depth  $h_0$ , cf. figure 1. Neglecting friction, different formulations for the inviscid solution to the problem exists. These are briefly discussed in subsection 2.1. Common to all of these formulations is that the velocity field  $(U_{\text{inviscid}}, V_{\text{inviscid}})$  under the solitary wave is derived from a potential  $\Phi$ :

$$U_{\text{inviscid}}(x, y, t) = \frac{\partial \Phi}{\partial x}(x, y, t) \quad V_{\text{inviscid}}(x, y, t) = \frac{\partial \Phi}{\partial y}(x, y, t). \quad (1)$$

The quantities in (1) are scaled by the water depth  $h_0$  and the shallow water speed  $\sqrt{gh_0}$ :

$$x = \frac{x^*}{h_0} \quad y = \frac{y^*}{h_0} \quad \Phi = \frac{\Phi^*}{\sqrt{gh_0}h_0} \quad t = \frac{t^*\sqrt{gh_0}}{h_0}, \quad (2)$$

where the asterisk \* designates dimensional quantities. In this idealized description, solitary waves propagate without change in shape and velocity. In reality, however, frictional effects slowly dissipate the energy of the solitary wave. As mentioned in the introduction, most of the dissipation happens in the viscous boundary layer at the bottom. In this bottom boundary layer the velocity profile decreases to zero in order to satisfy the no-slip boundary condition at the wall. The flow in this thin layer is described by the boundary layer equations which are presented in subsection 2.2. These boundary layer equations are then solved numerically, cf. subsection 3.1, in order to obtain an accurate velocity profile of the boundary layer under a solitary wave. As an illustration, some profiles of the horizontal velocity component in the boundary layer under a solitary wave are displayed in figure 2. In addition to the boundary layer equations, the incompressible Navier-Stokes equations used for the validation by direct numerical simulation are presented in subsection 2.2 for the present problem. The central question in the present context is then to decide if the solution of the boundary layer equations is linearly stable and, if not, which are the parameters governing its instability. Linear stability of flows, cf. subsection 2.3, is traditionally investigated by means of the Orr-Sommerfeld equation (43) Jordinson (1970); Orszag (1971); Van Stijn and Van De Vooren (1980) and/or the parabolic stability equation (48) Bertolotti et al. (1992); Herbert (1997). We present these two equations in subsections 2.4 and 2.5, respectively.

### 2.1 Inviscid solitary wave solutions

The third order approximate solution by Grimshaw (1971) for the potential  $\Phi$  in 1 has been used by Liu et al. (2007) and Vittori and Blondeaux (2008, 2011) for their computations of the boundary layer profile. The velocity  $(U_{\text{inviscid}}, V_{\text{inviscid}})$

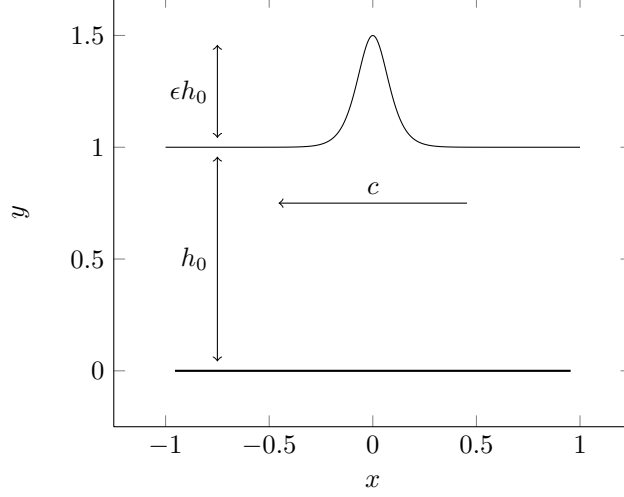


Figure 1: A solitary wave with height  $\epsilon h_0$  traveling from right to left on constant depth  $h_0$  at speed  $c$ . The axes are scaled according to (2).

is thereby approximated by Grimshaw (1971):

$$U_{\text{inviscid}} = -\epsilon s^2 \quad (3)$$

$$+ \epsilon^2 \left[ -\frac{1}{4}s^2 + s^4 + y^2 \left( \frac{3}{2}s^2 - \frac{9}{4}s^4 \right) \right] \quad (4)$$

$$+ \epsilon^3 \left[ \frac{19}{40}s^2 + \frac{1}{5}s^4 - \frac{6}{5}s^6 + y^2 \left( -\frac{3}{2}s^2 - \frac{15}{4}s^4 + \frac{15}{2}s^6 \right) \right] \quad (5)$$

$$+ y^4 \left( -\frac{3}{8}s^2 + \frac{45}{16}s^4 - \frac{45}{16}s^6 \right) \quad (6)$$

$$V_{\text{inviscid}} / (\sqrt{3\epsilon} y q) = -\epsilon s^2 \quad (7)$$

$$+ \epsilon^2 \left[ \frac{3}{8}s^2 + 2s^4 + y^2 \left( \frac{1}{2}s^2 - \frac{3}{2}s^4 \right) \right] \quad (8)$$

$$+ \epsilon^3 \left[ \frac{49}{640}s^2 - \frac{17}{20}s^4 - \frac{18}{5}s^6 + y^2 \left( -\frac{13}{16}s^2 - \frac{25}{16}s^4 + \frac{15}{2}s^6 \right) \right. \\ \left. + y^4 \left( -\frac{3}{40}s^2 + \frac{9}{8}s^4 - \frac{27}{16}s^6 \right) \right], \quad (10)$$

where

$$s = \text{sech}(\alpha(x + ct)), \quad q = \tanh(\alpha(x + ct)). \quad (11)$$

The wavenumber  $\alpha$  of the solitary wave is given by:

$$\alpha = \sqrt{\frac{3}{4}\epsilon} \left( 1 - \frac{5}{8}\epsilon + \frac{71}{128}\epsilon^2 \right), \quad (12)$$

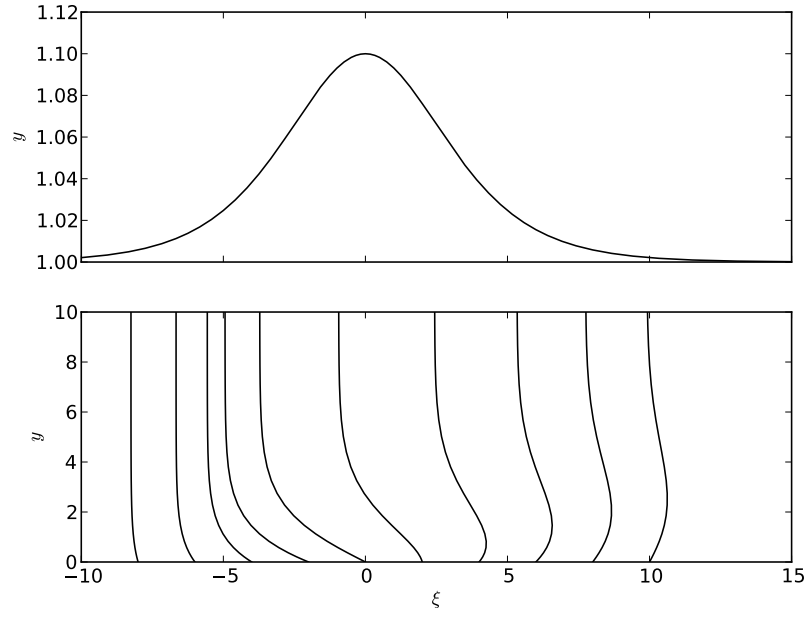


Figure 2: Surface elevation  $\eta$  and profiles of the horizontal velocity component in the boundary layer under a solitary wave moving from right to left,  $\epsilon = 0.1$ ,  $\delta = 8 \times 10^{-3}$ . The profiles have been multiplied by 40. Upper panel is scaled according to (2), while  $y$  in lower panel is scaled by (15).

and its celerity  $c$  by:

$$c^2 = 1 + \epsilon - \frac{1}{20}\epsilon^2 - \frac{3}{70}\epsilon^3. \quad (13)$$

Plots of the horizontal velocity profile under the crest of a solitary wave using the solution of Grimshaw (1971) and the full potential solution described below are given in figure 3. As can be observed from figure 3, the profile given by means of Grimshaw's solution deviates markedly from the full potential one for  $\epsilon > 0.2$ . For  $\epsilon > 0.3$  Grimshaw's profile does even qualitatively not follow the potential solution. Instead of increasing with the distance from the bottom, Grimshaw's profile decreases. The situation is, however, not as dramatic for the computation of the boundary layer flow, since in this case only the value of  $U_{\text{inviscid}}$  at the bottom is important. In figure 4,  $U_{\text{inviscid}}$  at the bottom wall is plotted for different values of  $\epsilon$ , the curves by Grimshaw's solution and the full potential solution are similar. However, for the  $\epsilon = 0.5$  case, for example, Grimshaw's solution overpredicts the magnitude of the bottom velocity under the crest of the solitary wave by approximately 7%. Hence, we instead use a numerical solution for the full potential  $\Phi$  by a method derived by Tanaka (1986) combined with a straightforward application of Cauchy's formula Pedersen et al. (2013). As mentioned above frictional effects will give rise to a thin viscous boundary layer at the bottom. The inviscid solution  $(U_{\text{inviscid}}, V_{\text{inviscid}})$  obtained by the method of Tanaka (1986) is then used to compute the boundary layer flow, equations (29-31), as described in the next subsection.

## 2.2 Navier-Stokes and Boundary layer equations

In the present work, we use two different scalings. The first one, (2), is based on the equilibrium water depth  $h_0$  as a length scale and the shallow water speed  $\sqrt{gh_0}$  as a velocity scale. The velocity scale for the second scaling is the same as for the first one. However, the length scale shall be given by  $\delta^*$ , which is a viscous length scale defined by Vittori and Blondeaux (2008, 2011), and which characterizes the thickness of the boundary layer:

$$\delta^* = \sqrt{\frac{2\nu h_0}{\sqrt{gh_0}}}. \quad (14)$$

Spatial variables are scaled by  $\delta^*$ :

$$x = x^*/\delta^*, \quad y = y^*/\delta^*. \quad (15)$$

We do not use different sub- or superscripts in order to label how variables are scaled. In general, in the remaining figures presented in this treatise the horizontal lengths are scaled by  $h_0$ , whereas the vertical lengths are scaled by  $\delta^*$ . As before velocities are scaled by  $\sqrt{gh_0}$ , which leads to time scaled the following way:

$$t = \frac{t^*\sqrt{gh_0}}{\delta^*}. \quad (16)$$



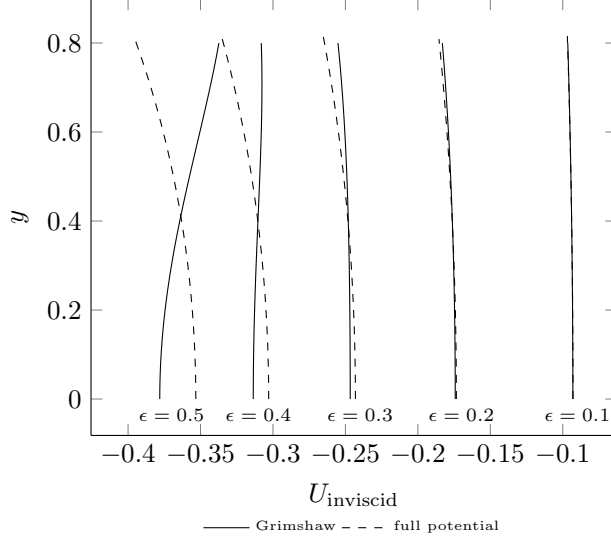


Figure 3: Profiles of the inviscid horizontal velocity  $U_{\text{inviscid}}$  under the crest of a solitary wave for different amplitudes  $\epsilon$ . The profiles have been computed by means of the third order approximate formula by Grimshaw (1971) and by means of the full potential solution solved by the method of Tanaka (1986). The scaling is given by (2).

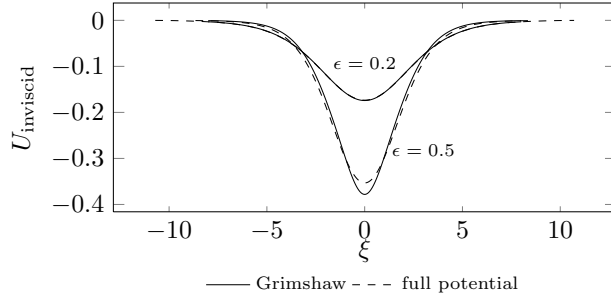


Figure 4: The inviscid horizontal velocity  $U_{\text{inviscid}}$  at the bottom wall for a solitary wave for different amplitudes  $\epsilon$ . The horizontal velocity has been computed by means of the third order approximate formula by Grimshaw (1971) and by means of the full potential solution solved by the method of Tanaka (1986). The scaling is given by (2).

The Navier-Stokes equations appear then as usual:

$$\frac{\partial u}{\partial x} + \frac{\partial v}{\partial y} = 0 \quad (17)$$

$$\frac{\partial u}{\partial t} + u \frac{\partial u}{\partial x} + v \frac{\partial u}{\partial y} = -\frac{\partial p}{\partial x} + \frac{1}{\text{Re}} \nabla^2 u \quad (18)$$

$$\frac{\partial v}{\partial t} + u \frac{\partial v}{\partial x} + v \frac{\partial v}{\partial y} = -\frac{\partial p}{\partial y} + \frac{1}{\text{Re}} \nabla^2 v, \quad (19)$$

where the Reynolds number  $\text{Re}$  is given by:

$$\text{Re} = \frac{\delta^* \sqrt{gh_0}}{\nu}. \quad (20)$$

Since  $\delta^*$  is a viscous length scale and given by (14), the Reynolds number can be further simplified.

$$\text{Re} = \frac{2h_0}{\delta^*} = \frac{2}{\delta}, \quad (21)$$

where  $\delta = \delta^*/h_0$ . Following Vittori and Blondeaux (2011) we will use  $\delta$  and  $\epsilon$  to identify the investigated cases. The list of employed  $\delta$  values, together with the corresponding value of  $h_0$  for water is

$\delta$	$1 \cdot 10^{-5}$	$4 \cdot 10^{-5}$	$8 \cdot 10^{-5}$	$1 \cdot 10^{-4}$	$4.75 \cdot 10^{-4}$	$8 \cdot 10^{-4}$
$h_0$ (m)	344.2	54.2	21.5	16.0	2.0	1.0

The smaller  $\delta$  corresponds to rather deep water, whereas the larger ones approach values that are relevant for wave tank experiments.

In order to derive the boundary layer equations an inhomogeneous scaling is used. The changes of the boundary layer flow in the horizontal direction happen on a length scale of  $h_0$ , whereas all variations of the boundary layer flow in the vertical direction are produced on a scale of  $\delta^*$ . The coordinates are therefore scaled the following way:

$$x = \frac{x^*}{h_0}, \quad y = \frac{y^*}{\delta h_0}. \quad (22)$$

The velocity components are scaled accordingly:

$$u = \frac{u^*}{\sqrt{gh_0}}, \quad v = \frac{v^*}{\sqrt{gh_0}\delta}. \quad (23)$$

When we insert this into the Navier-Stokes equations and retain only the leading order terms in  $\delta^2$  terms, we arrive at the following boundary layer equations:

$$\frac{\partial u}{\partial x} + \frac{\partial v}{\partial y} = 0, \quad (24)$$

$$\frac{\partial u}{\partial t} + u \frac{\partial u}{\partial x} + v \frac{\partial u}{\partial y} = -\frac{\partial p^{\text{ext}}}{\partial x} + \frac{1}{2} \frac{\partial^2 u}{\partial y^2}, \quad (25)$$

$$\frac{\partial p^{\text{ext}}}{\partial y} = 0, \quad (26)$$

where the exterior pressure gradient is given by the inviscid bulk flow:

$$-\frac{\partial p^{\text{ext}}}{\partial x} = \frac{\partial}{\partial t} U_{\text{inviscid}}(x, 0, t) + U_{\text{inviscid}}(x, 0, t) \frac{\partial}{\partial x} U_{\text{inviscid}}(x, 0, t). \quad (27)$$

However, the problem with equations (24-26) is that its solution is not steady and we would be constrained to redefine the notion of hydrodynamic stability as attempted in Sumer et al. (2010), Vittori and Blondeaux (2008, 2011) and Blondeaux et al. (2012). To avoid this difficulty and to be able to use classical hydrodynamic stability theory Drazin and Reid (1981), we employ a simple standard trick. Equations (17-18) are valid for an observer in the frame of reference defined by the equilibrium state. This observer sees a wave traveling with velocity  $-c \mathbf{e}_x$ . However, for the remainder of the present work the frame of reference will be defined by the solitary wave itself. The observer will then see a bottom moving at velocity  $c \mathbf{e}_x$  and water entering at velocity  $c \mathbf{e}_x$ . The letter  $\xi$  shall be used to denote the moving coordinate:

$$\xi = x + ct. \quad (28)$$

Since the Navier-Stokes equations are Galilean invariant they appear the same as in equations (17-18) with only  $x$  replaced by  $\xi$ . The Navier-Stokes equations in the moving frame of reference with both spatial variables scaled by  $\delta^*$  are then used for the Orr-Sommerfeld equation (43), the parabolic stability equation (48) and the Navier-Stokes solver, cf. subsection 3.4.

Neglecting the slow change of the inviscid base flow due to viscous dissipation, the boundary layer flow can be regarded as steady in this frame of reference. The final boundary layer equations are thus given by:

$$\frac{\partial u}{\partial \xi} + \frac{\partial v}{\partial y} = 0, \quad (29)$$

$$u \frac{\partial u}{\partial \xi} + v \frac{\partial u}{\partial y} = -\frac{\partial p^{\text{ext}}}{\partial \xi} + \frac{1}{2} \frac{\partial^2 u}{\partial y^2}, \quad (30)$$

$$\frac{\partial p^{\text{ext}}}{\partial y} = 0, \quad (31)$$

where the exterior pressure gradient is given by the inviscid bulk flow:

$$-\frac{\partial p^{\text{ext}}}{\partial \xi} = U_{\text{inviscid}}(\xi, 0) \frac{\partial U_{\text{inviscid}}}{\partial \xi}(\xi, 0). \quad (32)$$

The boundary conditions for (29-31) in the vertical direction are given by:

$$u = c \quad \text{at} \quad y = 0, \quad (33)$$

$$u = U_{\text{inviscid}}(\xi, 0) \quad \text{at} \quad y = y^{\text{ext}} \quad (34)$$

$$v = 0 \quad \text{at} \quad y = 0, \quad (35)$$

where  $y^{\text{ext}}$  is the 'edge' of the boundary layer Keller (1978). We solve equations (29-31) numerically by a Chebyshev collocation method. The details of this

method are presented in subsection 3.1. Once a solution to (29-31) has been found, we use linear stability to determine whether this boundary layer flow is stable or not. This boundary layer flow is thus the steady base flow for the remainder of this study. The solution of (29-31), marked by lower case letters  $u$  and  $v$ , shall subsequently be denoted by upper case letters

$$U_{\text{base}} \quad \text{and} \quad V_{\text{base}}. \quad (36)$$

The reason for this is to distinguish the boundary layer flow from the perturbed flow, which is the sum of the base flow and the perturbation as explained in the following subsection.

### 2.3 Linear stability of the boundary layer

An in-depth review on linear stability of boundary layers is given in the book by Drazin and Reid (1981). The following subsections give a brief overview of the equations needed herein.

Since our problem treated is two dimensional, the base flow, equation (36), can be derived from a stream function  $\Psi$  in the following way:

$$U_{\text{base}} = \frac{\partial \Psi}{\partial y} \quad V_{\text{base}} = -\frac{\partial \Psi}{\partial \xi}. \quad (37)$$

The pressure can then be eliminated from the Navier-Stokes equations (17-19) leading to a governing equation for the stream function  $\Psi$  White (2005):

$$\left( \frac{\partial}{\partial t} - \frac{1}{Re} \nabla^2 + \frac{\partial \Psi}{\partial y} \frac{\partial}{\partial \xi} - \frac{\partial \Psi}{\partial \xi} \frac{\partial}{\partial y} \right) \nabla^2 \Psi = 0. \quad (38)$$

A common ansatz in linear stability theory is to add a perturbation  $(u', v')$  to the base flow (37). As before we write this perturbation in stream function form:

$$u' = \frac{\partial \psi'}{\partial y} \quad v' = -\frac{\partial \psi'}{\partial \xi}. \quad (39)$$

Injecting now the perturbed flow  $\Psi + \psi'$  into (38), we obtain a nonlinear governing equation for the perturbation  $\psi'$ . Since, however, the perturbation is assumed to be small in amplitude, we can neglect the nonlinear terms and find a linear equation for the perturbation  $\psi'$  for a given base flow  $\Psi$ :

$$\left( \frac{\partial}{\partial t} - \frac{1}{Re} \nabla^2 + \frac{\partial \Psi}{\partial y} \frac{\partial}{\partial \xi} - \frac{\partial \Psi}{\partial \xi} \frac{\partial}{\partial y} \right) \nabla^2 \psi' + \frac{\partial \nabla^2 \Psi}{\partial \xi} \frac{\partial \psi'}{\partial y} - \frac{\partial \nabla^2 \Psi}{\partial y} \frac{\partial \psi'}{\partial \xi} = 0 \quad (40)$$

This equation is the foundation for the two methods of linear stability which shall be used in the present discussion. The first one is the famous Orr-Sommerfeld equation, cf. subsection 2.4, whereas the second one is the parabolic stability equation presented briefly in subsection 2.5.

## 2.4 Orr-Sommerfeld equation

The Orr-Sommerfeld equation, see Drazin and Reid (1981) for a more detailed review, is based on the assumption of parallel flow. This means that the normal component of the base flow is assumed to be negligible,  $V_{base} = -\partial\Psi/\partial x = 0$  and that non parallel effects are ignored. Hence, the stability of each profile for a given  $\xi$  is analyzed independently. The resulting governing equation for  $\psi'$  is thus given by:

$$\left( \frac{\partial}{\partial t} - \frac{1}{Re} \nabla^2 + \frac{\partial\Psi}{\partial y} \frac{\partial}{\partial \xi} \right) \nabla^2 \psi' - \frac{\partial^3 \Psi}{\partial y^3} \frac{\partial \psi'}{\partial \xi} = 0 \quad (41)$$

Looking at each profile independently means that we assume the perturbation to have a specific form. It is modeled as a Tollmien-Schlichting wave traveling along the horizontal direction:

$$\psi' = \phi(y) \exp(a\xi - i\omega t), \quad (42)$$

where  $\phi$  is an unknown function controlling the shape of the wave in normal direction. The given real number  $\omega$  is the angular velocity of the wave. The complex part of  $a$  is the wave number and its real part the growth rate of the wave. For a given angular velocity  $\omega$  and a given profile at some  $\xi$ , equation (41) gives rise to an algebraic eigenvalue problem for the eigenvalue  $a$  and the eigenfunction  $\phi$ , the famous Orr-Sommerfeld equation Drazin and Reid (1981):

$$\frac{1}{Re} (D^2 + a^2)^2 \phi + (i\omega - U_{base} a) (D^2 + a^2) \phi + \frac{\partial^2 U_{base}}{\partial y^2} a \phi = 0, \quad (43)$$

where  $D = d/dy$ . The boundary conditions for  $\phi$  are given by:

$$\phi(0) = D\phi(0) = 0 \quad \phi(y \rightarrow \infty) \rightarrow 0. \quad (44)$$

The discrete spectrum of (43) will determine the stability of the flow. If there exists an eigenvalue  $a$  with a positive real part, then we say that the base flow is (becoming) unstable. This happens usually at a certain value of  $\xi$  after which the Orr-Sommerfeld equation gives rise to eigenvalues with positive real part. The numerical details on how equation (43) is solved are given in subsection 3.2. Unstable regions along the horizontal axis  $\xi$  for a given  $\omega$  are then defined by:

$$\text{Re } a(\xi) > 0. \quad (45)$$

As in Jordinson (1970), amplification of the perturbation is measured by

$$\ln \frac{A}{A_0} = \int_{\xi_0}^{\xi} \text{Re } a(x) dx. \quad (46)$$

As shall be seen later on, the nonparallel effects are, however, significant for the present boundary layer. Therefore, an additional method of linear stability shall be used, the parabolic stability equation, presented in the next subsection.

## 2.5 Parabolic stability equation

The parabolic stability equation was derived by Bertolotti et al. (1992). An in-depth discussion of this method can be found in their article and in Herbert (1997). In the present subsection only a brief summary of the main elements is given. This method pursues two goals. First, it weakens the parallel flow assumption and only assumes that the flow is slowly varying in  $\xi$ . Second, it reformulates the governing equation as an initial value problem and not as an eigenvalue problem. As we do not assume that the base flow is parallel, the perturbation, equation (39) needs, opposed to the Orr-Sommerfeld equation, to account for a variation in  $\xi$ . Bertolotti et al. (1992) proposed the following ansatz for the Tollmien-Schlichting wave:

$$\psi' = \phi(\xi, y) \exp \left( \int_{\xi_0}^{\xi} a(\hat{\xi}) d\hat{\xi} - i\omega t \right). \quad (47)$$

Now the shape function  $\phi$  and the wave number and growth rate defined by  $a$  are dependent on  $\xi$ . Although the flow is not assumed to be parallel, it is assumed that all flow variables vary slowly with respect to  $\xi$ , such that higher than first order derivatives of  $\phi$  and  $a$  with respect to  $\xi$  can be neglected. This leads to the following nonlinear initial value problem for  $a$  and  $\phi$ , cf. Bertolotti et al. (1992):

$$(L_0 + L_1) \phi + L_2 \frac{\partial \phi}{\partial \xi} + L_3 \phi \frac{da}{d\xi} = 0, \quad (48)$$

where the operators  $L_i$ ,  $i = 0, 1, 2, 3$  operate on  $y$  only and are given by:

$$L_0 = -\frac{1}{Re} (D^2 + a^2)^2 + (i\omega - U_{base} a) (D^2 + a^2) - \frac{\partial^2 U_{base}}{\partial y^2} a, \quad (49)$$

$$L_1 = -\frac{\partial^2 V_{base}}{\partial y^2} D + V_{base} (D^2 + a^2) D, \quad (50)$$

$$L_2 = -\frac{4a}{Re} (D^2 + a^2) + U_{base} (D^2 + 3a^2) - 2i\omega a - \frac{\partial^2 U_{base}}{\partial y^2} \quad (51)$$

$$L_3 = -\frac{2}{Re} (D^2 + 3a^2) - i\omega + 3aU_{base} \quad (52)$$

The form of  $\psi'$ , equation (47), is not unique and an additional condition is needed to determine  $\phi$  and  $a$ . The main idea for finding an additional constraint is to restrict the growth to the parameter  $a$  and let  $\phi$  only have variations in shape. As mentioned by Bertolotti et al. (1992), several choices are possible. In the present discussion, we adopt one of their choices, namely to require orthogonality between the horizontal velocity component and its derivative with respect to  $\xi$  Bertolotti et al. (1992):

$$\int_0^\infty \frac{\partial^2 \phi}{\partial \xi \partial y} \frac{\partial \bar{\phi}}{\partial y} dy = 0. \quad (53)$$

In order to be able to measure the growth of the perturbation independently of the constraint chosen, Bertolotti et al. (1992) defined the amplitude  $A$  of the perturbation the following way:

$$A = \max_y \left| \frac{\partial \phi}{\partial y} \right| \exp \int_{\xi_0}^{\xi} \operatorname{Re} a(x) dx. \quad (54)$$

The amplification is then the ratio between the amplitudes at two different points:

$$\frac{A}{A_0} = \frac{\max_y \left| \frac{\partial \phi}{\partial y} \right| \exp \int_{\xi_0}^{\xi} \operatorname{Re} a(x) dx}{\max_y \left| \frac{\partial \phi_0}{\partial y} \right|}. \quad (55)$$

The unstable region along the horizontal axis for a given  $\omega$  is then bounded by the points  $\xi$ , where

$$\max_y \left| \frac{\partial \phi}{\partial y} \right| \exp \int_{\xi_0}^{\xi} a(x) dx \quad (56)$$

is minimum or maximum. The last term in equation (48) given by  $L_3 da/d\xi$  is neglected in Bertolotti et al. (1992) as well as in the present work. A back-calculation of the term after solution of the equations does indeed confirm that it is small.

### 3 Numerical methods

Since the present investigation depends crucially on the quality of the numerical analysis employed, we present a brief description of each numerical method used in this section.

#### 3.1 Boundary layer equations solver

In order to solve the boundary layer equations (29-30), we use a Chebyshev collocation method, cf. Trefethen (2000), since Chebyshev polynomials are superior in accuracy compared to classical finite difference formulations Orszag (1971). The problem (29-30) is then solved on a  $(N_{\text{BL}} + 1) \times (N_{\text{BL}} + 1)$  grid at the Gauß Lobatto Chebyshev knots. The differential operators in (29-30) are replaced by their discrete representations:

$$\frac{\partial}{\partial \xi} \leftrightarrow D_\xi = \frac{1}{L_x} D_N \otimes I, \quad (57)$$

$$\frac{\partial}{\partial y} \leftrightarrow D_y = I \otimes \frac{2}{y^{\text{ext}}} D_N, \quad (58)$$

$$\frac{\partial^2}{\partial y^2} \leftrightarrow D_y^2 = I \otimes \frac{4}{y^{\text{ext}2}} D_N^2, \quad (59)$$

where  $I$  is the identity matrix and  $D_N$  the Chebyshev collocation differentiation matrix. The lengths  $L_x$  and  $y^{\text{ext}}$  control the size of the domain  $[-L_x, L_x] \times [0, y^{\text{ext}}]$ . Once we are given, an initial guess  $u_N^0$  for the discrete solution  $u_N$ , we solve first the continuity equation for  $v_N^0$ :

$$A v_N^0 = b^0 \quad (60)$$

where  $A$  is essentially  $D_y$  and  $b$  is essentially  $-D_\xi u_N^0$ . The rows of  $A$  corresponding to the boundary  $y = 0$ , are modified in order to account for  $v_N^0 = 0$  at the lower boundary. The corresponding rows in  $b^0$  are modified accordingly. The construction of the momentum operator  $C$  is similar. First we set

$$C^0 = \text{diag}(u_N^0) D_\xi + \text{diag}(D_\xi u_N^0) + \text{diag}(v_N^0) D_y - \frac{1}{2} D_y^2, \quad (61)$$

where  $\text{diag}(u_N^0)$  designates a diagonal matrix with the elements of  $u_N^0$  on the diagonal. Some rows of  $C$  are modified in order to account for:

$$u_N^0 = c \quad \text{at} \quad \xi = 0 \quad (62)$$

$$u_N^0 = c \quad \text{at} \quad y = 0 \quad (63)$$

$$u_N^0 = U_{\text{inviscid}} \quad \text{at} \quad y = y^{\text{ext}} \quad (64)$$

The second member  $d$  is obtained similarly by posing:

$$d^0 = U_{\text{inviscid}} \frac{\partial U_{\text{inviscid}}}{\partial \xi} - \text{diag}(u_N^0) D_\xi u_N^0 - \text{diag}(v_N^0) D_\xi u_N^0 + \frac{1}{2} D_y^2 u_N^0. \quad (65)$$



As before, some elements of  $d$  need to be modified in order to account for the boundary conditions (62-64). The increment  $u'_N$  updating the solution  $u_N$  from  $u_N^0$  to  $u_N^1 = u_N^0 + u'_N$  is then computed by solving:

$$C^0 u'_N = d^0. \quad (66)$$

This procedure is iterated until the Euclidean norm of  $u'_N$  falls below  $10^{-12}$ . The result gives then the base flow  $(U_{\text{base}}, V_{\text{base}})$  we need for the methods described below. The code was written in MATLAB and we verified the above algorithm by a test problem as well as comparison with the boundary layer model of Pedersen et al. (2013), which again was compared to measurements. In addition the present boundary layer equations solver was validated by means of the Blasius boundary layer. The results of this benchmarking can be found in appendix A. The boundary layer solutions used in section 4 were all computed using a resolution of  $N_{\text{BL}} = 80$ , which gives sufficiently accurate results as can be verified in appendix A. The edge of the boundary layer, given by  $y^{\text{ext}}$ , is of course chosen such that the boundary layer width is smaller than  $y^{\text{ext}}$ . As a matter of fact the boundary layer width is often less than the width of the Tollmien-Schlichting waves. Therefore, we chose a larger than necessary value for  $y^{\text{ext}}$ , namely  $y^{\text{ext}} = 60$ , cf. appendix A, such that the bulk of the Tollmien-Schlichting waves fits into the domain. However, for very low frequencies the Tollmien-Schlichting wave displays a large width. Therefore an extrapolation of  $(U_{\text{base}}, V_{\text{base}})$  for values of  $y$  larger than  $y^{\text{ext}}$  is necessary. This is done by means of the inviscid solution  $(U_{\text{inviscid}}, V_{\text{inviscid}})$  in such a way that at  $y^{\text{ext}}$  the extrapolant is continuous in the horizontal and vertical velocity.

### 3.2 Orr-Sommerfeld equation solver

The numerical solution of the Orr-Sommerfeld equation has led to a vast number of works published in literature Osborne (1967); Jordinson (1970); Orszag (1971); Van Stijn and Van De Vooren (1980). In the following we use as in Orszag (1971) a Chebyshev collocation method in order to solve equation (43) in the domain  $[0, L_y]$ . We choose to cut the domain at  $L_y$  instead of using an algebra mapping. Once we are given the differentiation matrix  $D_N$ , the discrete version of equation (43) can be written as:

$$\begin{aligned} & - \frac{1}{Re} \left( \frac{16}{L_y^4} D_N^4 + \frac{8}{L_y^2} a^2 D_N^2 + a^4 I \right) \phi_N \\ & + (\text{diag}(U_{\text{base}})a - i\omega I) \left( \frac{4}{L_y^2} D_N^2 + a^2 I \right) \phi_N - a \text{diag} \left( \frac{\partial^2 U_{\text{base}}}{\partial y^2} \right) \phi_N = 0 \end{aligned} \quad (67)$$

where  $I$  is the identity matrix and  $\phi_N$  are the values of  $\phi$  at the  $N_{\text{OSE}} + 1$  Gauß Lobatto Chebyshev nodes. In order to solve (67) together with the boundary conditions (44) we use an approach described in Trefethen (2000). The fourth order differentiation matrix  $D_N^4$  in (67) is thereby replaced by a different matrix  $\tilde{D}_N^4$  which ensures the correct boundary conditions, see Trefethen

(2000) for details. The code was written in MATLAB. We used the method by Osborne (1967) and the inbuilt eigenvalue solver by MATLAB to solve the eigenvalue equation (67). This was done in order to double-check the correctness of the solution. As verification, some eigenvalues and eigenfunctions for the Blasius boundary value were computed using the present solver and the results were compared to values in literature, cf. appendix B. The important numerical parameters for the present Orr-Sommerfeld solver are the number  $N_{\text{OSE}}$  of Chebyshev collocation points and the extension of the domain  $L_y$ . The determination of the extension  $L_y$  for the Orr-Sommerfeld equation solver is opposed to the extension in  $y$  for the boundary layer equations solver in subsection 3.1 not determined by the thickness of the boundary layer but instead by the width of the Tollmien-Schlichting wave, which can be several times larger than the boundary layer thickness. As mentioned in Van Stijn and Van De Vooren (1980), the dominant asymptotic solution to the Orr-Sommerfeld equation for  $y \rightarrow \infty$  in case for the Blasius boundary layer is given by:

$$\phi \approx \exp(-\text{Im}(a)y), \quad (68)$$

where  $\phi$  and  $a$  are defined in (42). As we shall see in section 4, the phase speed of the Tollmien-Schlichting wave in the boundary layer under a solitary wave is close to the celerity  $c$  of the solitary wave. Assuming that the asymptotic solution (68) is also approximately valid for a the Tollmien-Schlichting wave in the boundary layer under a solitary wave, it allows us to give an apriori estimation of  $L_y$  by posing

$$L_y = c_{\text{TS}}/\omega, \quad (69)$$

where  $c_{\text{TS}}$  is a constant. By numerical inspection we found that a value of  $c_{\text{TS}} = 10$  allows enough tolerance to capture the Tollmien-Schlichting wave for a broad range of  $\epsilon$  and  $\delta$ . This value has been used for all simulations throughout the present treatise. The number  $N_{\text{OSE}}$  of Chebyshev collocation points has been determined by convergence tests, cf. appendix B, and is fixed to the value  $N_{\text{OSE}} = 130$  for the remainder of the present work.

### 3.3 Parabolic stability equation solver

For the parabolic stability equation solver, we use basically the same approach as in Bertolotti et al. (1992). The main difference is that instead of using an algebraic mapping in order to map the interval  $[-1, 1]$  onto  $[0, \infty)$ , we use truncation of the domain at  $L_y$ . In Grosch and Orszag (1977) it was shown that although truncation of the domain is less efficient than an algebraic mapping, it does nevertheless produce accurate results. As in Bertolotti et al. (1992), the operators  $L_0$ ,  $L_1$  and  $L_2$  are replaced by their discrete correspondence  $M_0$ ,  $M_1$

and  $M_2$ , respectively, defined the following way:

$$M_0 = -\frac{1}{Re} \left( \frac{16}{L_y^4} \tilde{D}_N^4 + \frac{8}{L_y^2} a^2 D_N^2 + a^4 I \right) + (\text{diag}(U_{\text{base}})a - i\omega I) \left( \frac{4}{L_y^2} D_N^2 + a^2 I \right) - a \text{diag} \left( \frac{\partial^2 U_{\text{base}}}{\partial y^2} \right) \quad (70)$$

$$M_1 = -\text{diag} \left( \frac{\partial^2 V_{\text{base}}}{\partial y^2} \right) \frac{2}{L_y} D_N + \text{diag}(V_{\text{base}}) \left( \frac{8}{L_y^3} \tilde{D}_N^3 + a^2 \frac{2}{L_y} D_N \right) \quad (71)$$

$$M_2 = -\frac{4a}{Re} \left( \frac{4}{L_y^2} D_N^2 + a^2 I \right) + \text{diag}(U_{\text{base}}) \left( \frac{4}{L_y^2} D_N^2 + 3a^2 I \right) - 2i\omega a I - \text{diag} \left( \frac{\partial^2 U_{\text{base}}}{\partial y^2} \right). \quad (72)$$

The discretization of (48) in  $x$  is then done as in Bertolotti et al. (1992) by using second order central finite differences:

$$(M_0 + M_1) \frac{1}{2} (\phi_{j+1} + \phi_j) + M_2 \frac{1}{\Delta \xi} (\phi_{j+1} - \phi_j) = 0. \quad (73)$$

As in Bertolotti et al. (1992), the operators  $M_0$ ,  $M_1$  and  $M_2$  in (73) are evaluated using the value of  $a$  at the midpoint, namely  $a_{\text{mid}} = (a_j + a_{j+1})/2$ . Since equation (73) is nonlinear in  $a_{j+1}$ , it is solved iteratively together with the constraint (53). A first guess  $a_{j+1}^0$  is given by  $a_j$ , this allows us to obtain an approximation  $\phi_{j+1}^0$  at the node  $\xi_{j+1}$  by solving (73). However,  $\phi_{j+1}^0$  does not necessarily obey (53). In order to obtain a new value  $a_{j+1}^1$ , we solve the following equation for the complex number  $\kappa$ :

$$\alpha \kappa \bar{\kappa} + \beta \kappa + \gamma \bar{\kappa} + \delta = 0. \quad (74)$$

This equation is the discrete form of (53) and the coefficients are given by

$$\alpha = \frac{1}{2(\xi_{j+1} - \xi_j)} \int_0^{L_y} dy \frac{\partial \phi_{j+1}^0}{\partial y} \overline{\frac{\partial \phi_{j+1}^0}{\partial y}} \quad (75)$$

$$\beta = \frac{1}{2(\xi_{j+1} - \xi_j)} \int_0^{L_y} dy \frac{\partial \phi_{j+1}^0}{\partial y} \overline{\frac{\partial \phi_j^0}{\partial y}} \quad (76)$$

$$\gamma = \frac{1}{2(\xi_{j+1} - \xi_j)} \int_0^{L_y} dy \overline{\frac{\partial \phi_{j+1}^0}{\partial y}} \frac{\partial \phi_j^0}{\partial y} \quad (77)$$

$$\delta = \frac{1}{2(\xi_{j+1} - \xi_j)} \int_0^{L_y} dy \frac{\partial \phi_j^0}{\partial y} \overline{\frac{\partial \phi_j^0}{\partial y}} \quad (78)$$

The differentiation with respect to  $y$  is as before done by means of the differentiation matrix  $D_N$ , whereas the integration with respect to  $y$  is done by means of a trapezoidal quadrature rule. Once the root  $\kappa$  is found we pose:

$$a_{j+1}^1 = a_{j+1}^0 + \frac{2}{\xi_{j+1} - \xi_j} \ln \kappa. \quad (79)$$

With this new result for  $a_{j+1}$ , we solve again (73) and repeat the procedure until convergence, which is obtained in our case when

$$|\frac{2}{\xi_{j+1} - \xi_j} \ln \kappa| < 10^{-8}. \quad (80)$$

The initial condition  $a_0$  and  $\phi_0$  is obtained by means of equation (26) in Bertolotti et al. (1992), which is an eigenvalue problem similar to the Orr-Sommerfeld equation (43). The program solving the parabolic stability equation has been written in MATLAB code and verified carefully. The results of this verification are presented in appendix C. There are three parameters governing the numerical accuracy of the method. These are given by

$$N_{\text{PSE}}, \quad \text{the number of Chebyshev collocation points in } y, \quad (81)$$

$$L_y, \quad \text{the extension of the domain in } y \text{ and} \quad (82)$$

$$\Delta\xi, \quad \text{the discretization in } \xi \text{ direction.} \quad (83)$$

Since all physical quantities are slowly varying in  $\xi$ , the parabolic stability equation solver is relatively insensitive to the discretization  $\xi$ . However, the number of Chebyshev collocation points  $N_{\text{PSE}}$  and the extension of the domain  $L_y$  are important parameters to the method. The extension  $L_y$  is as for the Orr-Sommerfeld equation solver determined by formula 69. The determination of  $N_{\text{PSE}}$  is done by convergence tests, cf. appendix C. From these tests we found that choosing  $N_{\text{PSE}} = 180$  allows us to be on the safe side concerning the accuracy of the present results. This value has been used for all simulations throughout the present treatise. For the computation of a neutral curve, such as the one displayed in figure 32, the minimum or maximum of equation (56) is found when the change in  $\xi$  is less than  $10^{-5}$ . For the amplification plots, such as the ones in section 4, it is enough to mention that the plotting accuracy in  $\xi$  needed to produce a smooth figure is by far more stringent than the numerical accuracy needed to make the error contribution by  $\Delta\xi$  subdominant to the error contribution by  $N_{\text{PSE}}$ .

### 3.4 Legendre-Galerkin spectral element Navier-Stokes solver

Results obtained by the Orr-Sommerfeld equation solver and the parabolic stability equation solver described in subsections 3.2 and 3.3, respectively, are compared to direct numerical simulations using the spectral element Navier-Stokes solver NEK5000 which Fischer et al. (2008) developed at the Argon National Laboratory. The solver is freely available. Since control of the accuracy is crucial to obtain correct growth rates of the Tollmien-Schlichting waves, a spectral method was preferred to a low order method such as the one used in Vittori and Blondeaux (2008, 2011). The NEK5000 solver is based on a Galerkin formulation of the Navier-Stokes equations (17-19). The method uses a standard P/P-2 formulation based at the Gauß Lobatto Legendre nodes for  $u$  and  $v$  and the Gauß Legendre nodes for  $p$  Canuto et al. (1993). Convective and diffusive parts

are advanced in time by a splitting scheme. Nonlinear terms are integrated using Orszag's 3/2 rule. The pressure is solved by an Uzawa algorithm. Since the domain is rectangular a fast tensor product solver is used which increases the efficiency dramatically. More details on the implementation can be obtained in the documentation in Fischer et al. (2008).

In the present treatise we use for the direct numerical simulation an approach akin to the one developed by Fasel (1976). The set up used is sketched in figure 5. The domain is rectangular and aligned with the lower boundary of the computational domain. Since the frame of reference is moving with the solitary wave, the wall has a velocity ( $u = c, v = 0$ ), given by the speed of the solitary wave. The upper boundary is situated at  $y = L_y$ , where  $L_y$  is given by (69). The velocity needed for the velocity boundary condition at the upper boundary is obtained by  $(U_{\text{base}}, V_{\text{base}})$  computed in beforehand by means of the boundary layer solver. The right boundary of the domain at  $\xi = \xi_1$  is a simple outflow boundary with the condition  $p = 0$ . The left boundary condition is a velocity inlet at  $\xi = \xi_0$ , where we in addition to the base flow add a Tollmien-Schlichting wave  $(u', v')$ . The velocity  $(u, v)$  at the inflow is thus given by:

$$u = U_{\text{base}} + u' \quad v = V_{\text{base}} + v', \quad (84)$$

where  $U_{\text{base}}$  and  $V_{\text{base}}$  is the boundary layer flow and computed by the boundary layer solver in subsection 3.1. This approach to introduce the perturbation in the direct numerical simulation was first developed by Fasel (1976). In the present case, the perturbation  $(u', v')$  is computed by means of the parabolic stability equation:

$$u' = A_0 \left( \frac{\partial \text{Re}(\phi)}{\partial y} \cos(\text{Im}(a)\xi_0 - \omega t) - \frac{\partial \text{Im}(\phi)}{\partial y} \sin(\text{Im}(a)x_0 - \omega t) \right) \quad (85)$$

$$v' = A_0 \text{Im}(a) (\text{Re}(\phi) \sin(\text{Im}(a)x_0 - \omega t) + \text{Im}(\phi) \cos(\text{Im}(a)\xi_0 - \omega t)) \quad (86)$$

where  $\phi$  and  $a$  are given by equation (47). The amplitude is controlled by  $A_0$ , which is set to  $5 \cdot 10^{-4}$  for all simulations in order to make the perturbation small with respect to the mean flow, which is of order 1. An example of  $\phi$  obtained by means of the parabolic stability equation solver can be seen in figure 6. We remark that we neglected in (85) and (86) the terms due to the growth rate, the real part of  $a$ . However, this is not crucial, since it is small compared to the remaining parts. Another way of introducing  $(u', v')$  at the inflow would be to use only:

$$u' = A_0 \frac{\partial \text{Re}(\phi)}{\partial y} \cos(\text{Im}(a)\xi_0 - \omega t), \quad (87)$$

$$v' = A_0 \text{Im}(a) \text{Re}(\phi) \sin(\text{Im}(a)\xi_0 - \omega t), \quad (88)$$

as was done in Fasel (1976). By anticipating a few results from section 4, we tried this approach and it lead to a wrong amplification of the Tollmien-Schlichting wave in a region behind the inflow as it did in Fasel (1976). In the rest of the computational domain the amplification was, however, correct. Presumably, the

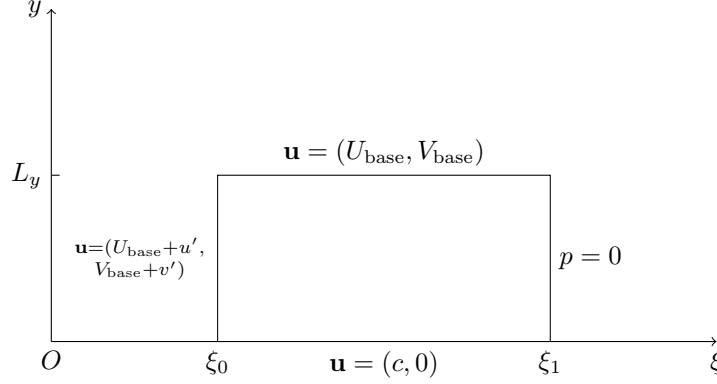


Figure 5: Set up for the Navier-Stokes solver

Tollmien-Schlichting wave introduced at the inflow by means of (87) and (88) needs to develop to the correct shape during a few wavelengths. This behaviour has been utilized by Bertolotti et al. (1992) for their direct numerical simulations. They used a generic shape mimicking a Tollmien-Schlichting wave to introduce the perturbation which then over a few wavelengths developed to the correct solution. As long as the frequency  $\omega$  of the perturbation generating the Tollmien-Schlichting wave in the direct numerical simulation is the same, the amplification of the Tollmien-Schlichting waves a few wavelengths downstream will be little affected by the details in its introduction.

The degree  $P$  of the polynomials and the number  $N_x, N_y$  of elements in  $\xi$  and  $y$  direction, respectively, are important for the numerical accuracy of the simulations. A first verification of the Navier-Stokes solver consists in testing the convergence of the solver when setting  $u' = v' = 0$ . In this case the results can be compared to the results computed by the boundary layer equations solver, cf. section 3.1. This verification is presented in appendix D. The length  $L_y$  is as for the Orr-Sommerfeld and the parabolic stability equation solver determined by the width of the Tollmien-Schlichting wave, equation (69). Increasing the degree  $P$  of the polynomials gives better agreement between the amplification computed by the Navier-Stokes solver and by the parabolic stability equation solver. For the results in section 4, we chose to work with  $P = 11$ . Although the boundary layer flow is slowly changing in  $\xi$ , the Tollmien-Schlichting wavelength is short, which makes it necessary to have similar spatial resolutions in  $\xi$  and  $y$ . For the results presented in section 4, we used  $N_x = 300$  elements in  $\xi$  direction for the cases with  $\delta = 8 \cdot 10^{-4}$  and  $\delta = 4.75 \cdot 10^{-4}$  and  $N_x = 600$  for the case with  $\delta = 10^{-4}$  since its domain has twice the size in  $\xi$  as compared to the other cases. In the  $y$  direction,  $N_y = 12$  elements were used in all simulations.

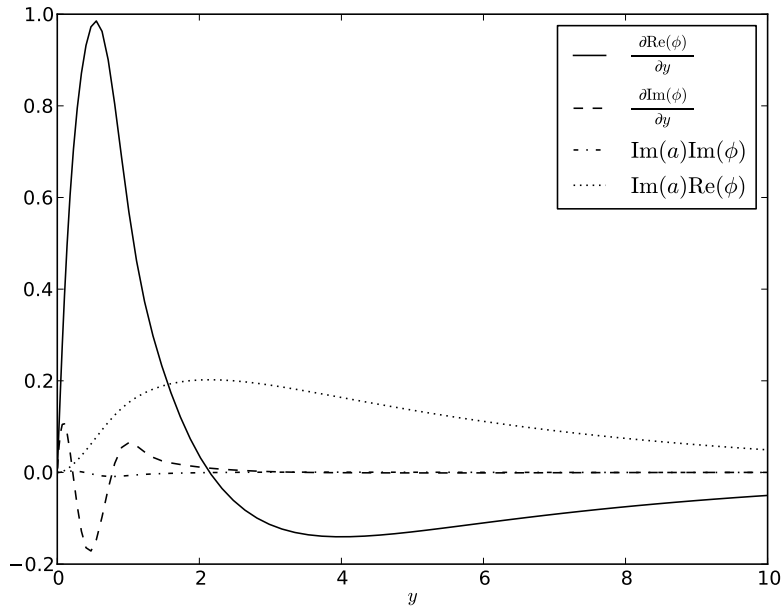


Figure 6: Profiles of the perturbation used for the Navier-Stokes solver, cf. equations (85) and (86). The parameters are  $\epsilon = 0.4$ ,  $\delta = 4.75 \cdot 10^{-4}$  and  $\omega = 0.22$  and the profile was taken at position  $\xi = -0.2375$ . The profiles are only shown to a value of the ordinate of  $y = 10$ . However, for the present case  $L_y = 45.5$ , a value at which the profiles have decayed sufficiently. The scaling for the  $y$  axis is given by (15).

## 4 Results

The results of the present analysis are divided into two parts. First, we discuss the linear and nonlinear boundary layer solutions in Liu et al. (2007) in connection with the erroneous formula presented in Liu and Orfila (2004), cf. subsection 4.1. Second, the general stability properties of the boundary layer flow under a solitary wave are presented in subsection 4.2.

### 4.1 Comparisons between linear and nonlinear boundary layer solutions

In Liu and Orfila (2004) the parameter corresponding to  $\delta$  is denoted by  $\alpha$  and includes a parameter controlling the dispersion of the solitary wave. Dispersion is less of an issue for the analysis of the boundary layer stability, such that we follow the parameter choice by Vittori and Blondeaux (2008). Changes in the boundary layer flow along the horizontal direction appear on a scale of  $h_0$ , whereas changes in vertical direction happen on a scale of  $\delta^*$ . For this parameter choice the corresponding inhomogeneous scaling in Liu and Orfila (2004) would be given by the following expressions.

$$x = \frac{x^*}{h_0}, \quad y = \frac{y^*}{\delta h_0}. \quad (89)$$

The velocity components are scaled accordingly:

$$u = \frac{u^*}{\epsilon \sqrt{gh_0}}, \quad v = \frac{v^*}{\epsilon \delta \sqrt{gh_0}}. \quad (90)$$

The expansion given in equations (2.7) and (2.8) in Liu and Orfila (2004), may then be written:

$$u = \frac{\partial \tilde{\Phi}}{\partial x} + u_0^r + \delta u_1^r + \dots, \quad (91)$$

$$v = \frac{\partial \tilde{\Phi}}{\partial y} + v_0^r + \delta v_1^r + \dots, \quad (92)$$

where the superscript  $r$  means that the velocity field is not irrotational. We remark that  $\tilde{\Phi}$  is a different mathematical object than the flow potential in (1). The potential  $\tilde{\Phi}$  represents the whole velocity field in the bulk of the fluid including the entrainment velocity induced by the viscous boundary layer, as explained in Liu and Orfila (2004). In addition the scaling of  $\tilde{\Phi}$  is different than the one in (1). Introducing this expansion into the Navier-Stokes equations (17-18) and neglecting terms of order  $\delta$ , we are given a set of equations for  $u_0^r$  and



$v_0^r$ :

$$\frac{\partial}{\partial x} u_0^r + \frac{\partial}{\partial y} v_0^r = 0, \quad (93)$$

$$\begin{aligned} \frac{\partial}{\partial t} u_0^r + \epsilon \left( \frac{\partial}{\partial x} \tilde{\Phi} \frac{\partial}{\partial x} u_0^r + u_0^r \frac{\partial^2}{\partial x^2} \tilde{\Phi} + u_0^r \frac{\partial}{\partial x} u_0^r \right. \\ \left. + \frac{\partial}{\partial y} \tilde{\Phi} \frac{\partial}{\partial y} u_0^r + v_0^r \frac{\partial^2}{\partial y \partial x} \tilde{\Phi} + v_0^r \frac{\partial}{\partial y} u_0^r \right) = \frac{1}{2} \frac{\partial^2}{\partial y^2} u_0^r. \end{aligned} \quad (94)$$

From equation (94), we observe that in equation (2.11) in Liu and Orfila (2004) the terms containing  $\tilde{\Phi}$  have been omitted. This is not so much of an issue for the work in Liu and Orfila (2004), since Liu and Orfila (2004) continued their analysis with the linearized equations in  $\epsilon$ . However, for the investigation of the boundary layer flow under a solitary wave in Liu et al. (2007) it is of importance. The entire part on the nonlinear boundary layer solution in Liu et al. (2007) is based on equation (2.11) in Liu and Orfila (2004) and needs therefore to be modified. The conclusions for the nonlinear boundary layer solution drawn on the basis of this analysis are not correct. In particular their statements that for large values of  $\epsilon$  the differences in the linear and nonlinear boundary layer solutions are 'not very significant' and the profiles are 'surprisingly close' need to be reconsidered. The present subsection shall elucidate this issue.

Opposed to the nonlinear boundary layer solution, the linear boundary layer solution for the horizontal velocity component in Liu et al. (2007) is correct and given by:

$$u_0^r(x, y, t) = -\frac{y}{\sqrt{2\pi}} \int_0^t \frac{\partial \Phi}{\partial x}(x, 0, \tau/2) \frac{e^{-\frac{y^2}{2(t-\tau)}}}{\sqrt{(t-\tau)^3}} d\tau, \quad (95)$$

where  $\Phi$  is the inviscid base flow as in equation (1). However, the boundary conditions for the linear wall normal velocity component in Liu et al. (2007) are wrong. As for the Blasius boundary layer, the boundary layer will displace fluid and therefore the condition

$$v_0^r \rightarrow 0 \quad \text{for} \quad y \rightarrow \infty \quad (96)$$

in Liu et al. (2007) is not correct and  $v_0^r$  cannot satisfy the impermeability condition  $v_0^r = 0$  at the wall and condition (96) at the same time. The condition (96) is, however, correct in Liu and Orfila (2004), since there,  $\partial \tilde{\Phi} / \partial y$  accounts for the displacement of fluid by the boundary layer. The solution for  $v_0^r$  given by equation (2.20) in Liu et al. (2007) needs therefore to be replaced by

$$v_0^r(x, y, t) = -\frac{1}{\sqrt{2\pi}} \int_0^t \frac{\partial^2 \Phi}{\partial x^2}(x, 0, \tau/2) \frac{1}{\sqrt{(t-\tau)}} \left( e^{-\frac{y^2}{2(t-\tau)}} - 1 \right) d\tau. \quad (97)$$

Liu et al. (2007) reported excellent agreement between their experimental results and their theoretical analysis. In particular they presented profiles for the case

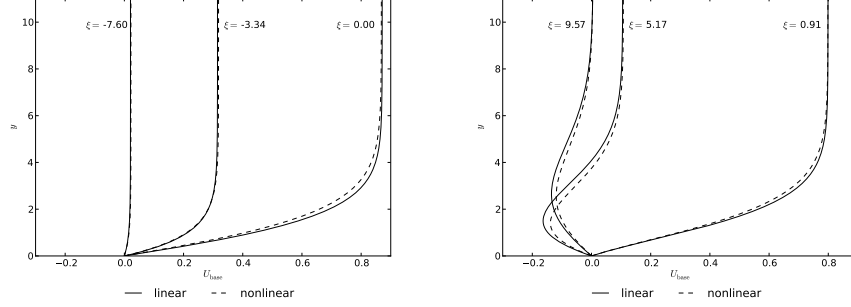


Figure 7: Profiles of the horizontal velocity for the case  $\epsilon = 0.2$  taken at different values of  $\xi$ . The linear profile is computed by means of equation (95), whereas the nonlinear profile is computed using equations (29) and (30). The scaling is given by (89) and (90).

$\epsilon = 0.2$  and  $\delta = 4.4 \cdot 10^{-3}$  at different locations  $\xi$ . The values of  $\xi$  in their scaling (i.e.  $\xi = 0.5, 0.22, -0.06, -0.34, -0.63$ ) correspond in the present scaling to the values  $\xi = -7.6, -3.34, 0.91, 5.17$  and  $9.57$ . In figures 7, 8 and 9, we plotted the profiles at these locations and under the crest  $\xi = 0$  using the linear solution, equation (95), and the nonlinear solution by the present boundary layer solver, cf. subsection 3.1, for the cases  $\epsilon = 0.2, 0.3$  and  $0.5$  respectively. As can be observed from these figures, qualitatively the linear and nonlinear profiles are displaying the same behavior for all values of  $\epsilon$ . However, quantitative differences arise already for a value of  $\epsilon = 0.2$ . The difference between the linear and nonlinear profiles is largest for the position  $\xi = 5.17$ . This is not surprising, since the flow in the boundary layer reverses its direction here. Convection has an influence in the sense that it softens the linear effect such that the profiles become less extreme. This effect can also be seen in the experimental results presented in figure 9 in Liu et al. (2007), where the experimental profile for  $\xi = 5.17$  ( $\xi = -0.34$  in their scaling) displays a softer bend than the nonlinear profile by Liu et al. (2007). Increasing the amplitude leads to increasing differences between the linear and the nonlinear solutions. As a measure of the difference, the maximum difference between each profile can be computed and compared to  $\epsilon$ . This will result into an error of 4% for the case  $\epsilon = 0.2$ , 5% for  $\epsilon = 0.3$  and 10% for  $\epsilon = 0.5$ . This is, however, a rather coarse estimation of the error, but gives a first indication on which differences to expect when comparing results based on linear or nonlinear profiles. Although, Liu et al. (2007) mentioned that they performed experiments for  $\epsilon = 0.3$ , they did not present results for this case.

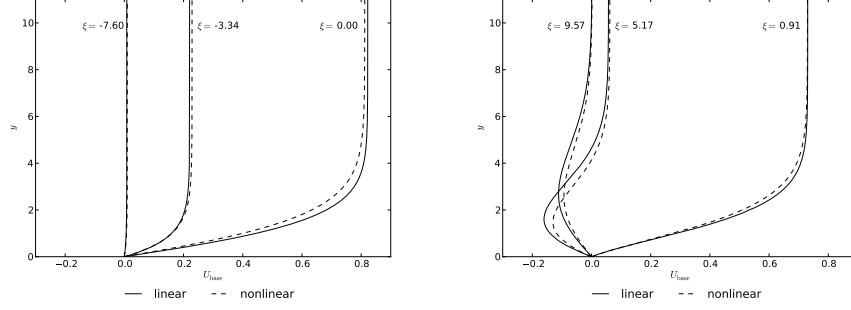


Figure 8: Profiles of the horizontal velocity for the case  $\epsilon = 0.3$  taken at different values of  $\xi$ . The linear profile is computed by means of equation (95), whereas the nonlinear profile is computed using equations (29) and (30). The scaling is given by (89) and (90).

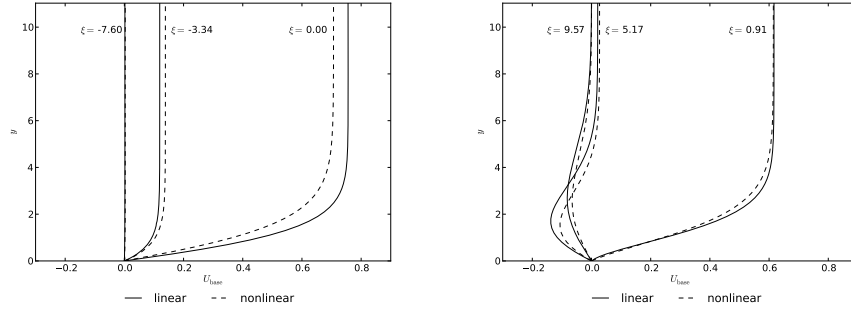


Figure 9: Profiles of the horizontal velocity for the case  $\epsilon = 0.5$  taken at different values of  $\xi$ . The linear profile is computed by means of equation (95), whereas the nonlinear profile is computed using equations (29) and (30). The scaling is given by (89) and (90).

## 4.2 Linear stability of the boundary layer flow under a solitary wave

In the present treatise, three different methods have been chosen to investigate the linear stability of the boundary layer flow under a solitary wave. The methods can be ranged by physical complexity, meaning the amount of physical effects their model includes. On a first level, we have the Orr-Sommerfeld equation solver, neglecting the nonparallel effects of the flow and nonlinear interactions of the perturbation. The parabolic stability equation, on the other hand, belongs as the Orr-Sommerfeld equation to the class of model equations, but includes effects of nonparallelism. However, also here nonlinear interactions of the perturbation are neglected. The Navier-Stokes solver is on the highest level, based on first principles for an incompressible Newtonian fluid. It accounts for all physical effects in the flow. As the amplitude of the perturbation is considered small, the parabolic stability equation solver and the Navier-Stokes solver are expected to produce similar results, since they both contain all the essential physics of the problem. This has been observed by Bertolotti et al. (1992) and Joslin et al. (1993) in their stability analysis of the Blasius boundary layer.

Figure 10 shows three plots for the case  $\epsilon = 0.4$  and  $\delta = 8 \cdot 10^{-4}$ . In figure 10(a), the stability domain of the flow, computed using the parabolic stability equation solver, has been plotted by means of criterion (56). For the region in  $(\xi, \omega)$  bounded by the neutral curve, Tollmien-Schlichting waves start to grow and may destabilize the flow. For the region outside of the neutral curve, the flow is stable and perturbations decay. At the neutral curve there is neither growth nor decay of the perturbations. The position  $\xi_c$  leftmost on the neutral curve is called the critical position, since for  $\xi > \xi_c$  perturbations are expected to grow. We now might pick a particular frequency  $\omega$  and follow the evolution of a Tollmien-Schlichting wave with this frequency. As a matter of fact the discrete spectrum of the Orr-Sommerfeld equation and the initial condition for the parabolic stability equation solver allows for an infinity of such Tollmien-Schlichting waves. Among these Tollmien-Schlichting waves, we always choose the most destabilizing one, meaning the one with maximum real part of  $a$ . To ease the discussion, we shall call the most destabilizing Tollmien-Schlichting wave simply the Tollmien-Schlichting wave in the following. In figure 10(b), we have chosen the Tollmien-Schlichting wave with the critical frequency  $\omega_c = 0.24$ . Dumping the velocity field  $u(\xi, y, t)$  from the Navier-Stokes solver at a specific point in time  $t$ , allows us to compute the perturbation velocity  $u'(\xi, y, t)$  by subtracting the base flow  $U_{\text{base}}(\xi, y)$  from the velocity field:

$$u' = u - U_{\text{base}}. \quad (98)$$

In figure 10(b), a slice of  $u'$  at  $y = 0.4943$  is plotted. We clearly observe a sinusoidal wave which decays until it reaches the critical position  $\xi_c = 0.82$  and then starts to grow, albeit slowly at the beginning. This qualitative picture can be analyzed further. Using the solution  $u(x, y, t)$  by the Navier-Stokes solver, we compute the amplitude of the Tollmien-Schlichting wave by means of the

envelope of  $u'$  at its maximum, i.e.:

$$A(\xi) = \max_{t,y} |u'(\xi, y, t)|. \quad (99)$$

This envelope can then be compared to the resulting amplifications using the parabolic stability equation, and the Orr-Sommerfeld equation, computed by means of equations (55) and (46), respectively. The result of this comparison is depicted in figure 10(c). All three methods predict first a decay of the Tollmien-Schlichting wave followed by growth. The results by the Navier-Stokes solver and by the parabolic stability equation solver agree remarkably well. This corresponds to the good agreement between the Navier-Stokes solver and the parabolic stability equation solver reported for the Blasius boundary layer mentioned above Bertolotti et al. (1992); Joslin et al. (1993). The results by the Orr-Sommerfeld solver on the other hand display an earlier growth of the Tollmien-Schlichting wave compared to the other two solvers. This indicates that nonparallel effects are significant and lead to quantitative differences.

Instead of choosing the critical frequency  $\omega_c$ , we might choose any other frequency, say  $\omega = 0.82$ , cf. figure 11. As can be seen from figure 11(a), the Tollmien-Schlichting wave for  $\omega = 0.82$  crosses the neutral curve twice. It enters the unstable region at  $\xi_a = 3.52$  and leaves it at  $\xi_b = 4.48$ . The wave is thus expected to first decay until  $\xi_a$ , to grow subsequently until  $\xi_b$ , and to decay again. This can also be seen by  $u'$  computed by means of the Navier-Stokes solver in figure 11(b). All three methods predict first decay of the wave, followed by growth and then decay again, cf. figure 11(c). The amplification computed by means of the Navier-Stokes solver and by means of the parabolic stability equation solver agree again remarkably well. As before the Orr-Sommerfeld solver predicts a somewhat different amplification of the Tollmien-Schlichting wave.

Also for other cases, a remarkably good agreement between Navier-Stokes results and results by the parabolic stability equation solver can be observed. In figures 12 and 13, we displayed the amplification by the three methods for the cases  $\epsilon = 0.4$ ,  $\delta = 4.75 \cdot 10^{-4}$ ,  $\omega = 0.22$  and  $\epsilon = 0.4$ ,  $\delta = 10^{-4}$ ,  $\omega = 0.185$ , respectively. The chosen frequencies correspond to the critical cases. As before the amplification by the Orr-Sommerfeld solver displays an earlier growth of the instability. However, for decreasing  $\delta$ , the difference becomes smaller. This is not surprising, since the vertical velocity component in the boundary layer scales like  $\delta$  and so do the nonparallel effects. For the  $\epsilon = 0.4$ ,  $\delta = 10^{-4}$ ,  $\omega = 0.185$  case, the critical position  $\xi_c$  is in the acceleration region of the flow ( $\xi < 0$ ), as can be seen from figure 13, we shall discuss this feature in a few lines below. The good agreement between Navier-Stokes solver and parabolic stability equation solver encourages us to continue the present stability analysis mainly by means of the parabolic stability equation solver.

In figures 14, 15, and 16 the stability domains in the  $(\xi, \omega)$  plane for the values of  $\delta = 8 \cdot 10^{-4}$ ,  $4.75 \cdot 10^{-4}$  and  $8 \cdot 10^{-5}$ , respectively, are displayed for different values of  $\epsilon$ . We observe that for the values of  $\delta = 8 \cdot 10^{-4}$  and  $\delta = 4.75 \cdot 10^{-4}$  all unstable regions are situated completely in the decelerating region of the

flow. This is the region where the pressure gradient  $dp^{\text{ext}}/d\xi$  is favorable for instability. Although the method for linear stability by Blondeaux et al. (2012) is derived for unsteady flows and growth in time, their unstable regions in the  $(\xi, k)$  plane, where  $k$  is the chosen wavenumber, are also entirely situated in the deceleration region, which supports the present result. As mentioned by Sumer et al. (2010), instability can be expected in this region of the flow, since the profile  $U_{\text{base}}$  displays an inflection point behind the crest, i.e. in the domain  $\xi > 0$ . Rayleigh's inflection point theorem is, however, not entirely applicable for the present case, since non-parallel effects are not negligible and viscosity plays an important role for the growth of the perturbation. Not surprisingly, the regions become larger for increasing amplitude  $\epsilon$  and decreasing  $\delta$ . Viscosity is thus a stabilizing factor. For  $\delta = 10^{-4}$  and smaller, cf. figure 16, we observe that the unstable region even grows beyond the line  $\xi = 0$  into the region of accelerated flow. Figure 17 shows how the stability domain evolves for  $\epsilon = 0.4$ , when  $\delta$  is decreased. The unstable domain forms a 'tongue', for lower values of  $\omega$ , reaching into the  $\xi < 0$  region for decreasing  $\delta$ . This 'tongue' is probably of viscous nature, since Rayleigh's stability criterion (although only valid for strictly parallel flows) does not allow for instability in this region. As such the form of this tongue is reminiscent of the unstable region of the Blasius boundary layer Drazin and Reid (1981). There is reason to believe that the instability mechanism in this case is similar to the one of the Blasius boundary layer Baines et al. (1996).

In order to estimate the significance of nonparallel effects, we computed the stability domains for the present boundary layer flow using the Orr-Sommerfeld equation for the cases  $\epsilon = 0.4$  and  $\delta = 8 \cdot 10^{-4}, 4.75 \cdot 10^{-4}, 10^{-4}$ . The results, in comparison to the ones by the parabolic stability equation, are plotted in figures 18 and 19. As also observed for individual frequencies above, the Orr-Sommerfeld equation predicts an earlier growth of the instability. As before, the difference between the unstable regions computed by means of the Orr-Sommerfeld and the parabolic stability equation becomes, however, smaller for smaller  $\delta$ . Although there are differences, the results by the two methods are still in good agreement, which supports the correctness of the present approach. Sumer et al. (2010) observed that irregular signals in the boundary layer can appear in front of the crest for higher Reynolds numbers  $Re_{\text{Sumer}}$ . In particular they presented the case  $Re_{\text{Sumer}} = 2 \cdot 10^6$ , cf. figure 10 (d) in Sumer et al. (2010), in which instabilities are observable for  $\xi < 0$ . In figure 20, the stability domains for different values of  $\epsilon$  and  $\delta$  are plotted. The values of  $\epsilon$  and  $\delta$  are chosen such that the cases correspond approximately to  $Re_{\text{Sumer}} = 2 \cdot 10^6$ . In order to convert between  $(\epsilon, \delta)$  and  $Re_{\text{Sumer}}$ , we use the conversion formula given in Vittori and Blondeaux (2011):

$$Re_{\text{Sumer}} = \frac{4}{\sqrt{3}} \frac{\epsilon^{3/2}}{\delta^2}. \quad (100)$$

From figure 20, we observe that the unstable region is not yet crossing the line  $\xi = 0$  for different values of  $\epsilon$  and  $\delta$  corresponding to  $Re_{\text{Sumer}} = 2 \cdot 10^6$ . Sumer et al. (2010) suspected turbulent spots to appear before  $\xi < 0$  for this Reynolds

number. This is not only in contrast to the present results indicating that Tollmien-Schlichting waves start growing only after passage of the crest for this case, but also to the works by Vittori and Blondeaux (2008, 2011) who found that for even bigger Reynolds numbers  $Re_{\text{Sumer}}$ , the region of instability is always located behind the crest. There are qualitative distinctions in the different analyses which need to be mentioned. Sumer et al. (2010), Vittori and Blondeaux (2008, 2011) and Blondeaux et al. (2012) considered temporal growth of instabilities, whereas in the present discussion we focus on spatial growth. One important distinction between the three different works is the velocity profile used. The velocity profile in the boundary layer in the experiments by Sumer et al. (2010) and in the simulations in Blondeaux et al. (2012) followed from a free stream flow in the form of a simple  $\text{sech}^2(\omega t)$  profile. Vittori and Blondeaux (2008, 2011), on the other hand, invoked Grimshaw's solution Grimshaw (1971) for the outer flow, which is better than the  $\text{sech}^2(\omega t)$  profile, but still deviates markedly from the exact one for higher amplitudes. Even more important, in all these references the approximation of spatially uniform free stream flow was made, which corresponds to the linear boundary layer solution by Liu et al. (2007), equation (95), since the nonlinear term vanishes. In the present discussion the velocity profile is the result of the nonlinear boundary layer equations (29-31) using a fully nonlinear solution of the potential equations. As shall be discussed below, Vittori and Blondeaux (2008, 2011) (and also Sumer et al. (2010) in their experiments) did not directly control the amplitude of the perturbation which might lead to a retarded appearance of the instability in their simulations. We doubt, however, that this is the reason for the discrepancy between the results of Vittori and Blondeaux (2008, 2011) and Sumer et al. (2010) for the  $Re_{\text{Sumer}} = 2 \cdot 10^6$  case. In figure 21, we plotted together with the results based on the full potential solution, stability domains for the linearized boundary layer profile by Liu et al. (2007), equation (95) with the correct formula for the normal velocity component, equation (97) by means of the parabolic stability equation solver. As can be seen the unstable region starts earlier for the linearized profile than for the fully nonlinear profile. In addition the critical frequency  $\omega_c$  is different than for the nonlinear case. Nevertheless, it does not extend into the acceleration region of the flow. Therefore, we believe that the discrepancy between the results by Vittori and Blondeaux (2008, 2011) and Sumer et al. (2010) for this case might be due to some disturbance in the experiments for higher  $Re_{\text{Sumer}}$ . We do, however, support the general observation by Sumer et al. (2010), that instability can occur in the acceleration region of the flow. This occurs, however, for higher Reynolds numbers  $Re_{\text{Sumer}}$  than theirs. In figure 17, the unstable region for the case  $\epsilon = 0.4$ ,  $\delta = 10^{-4}$  enters the acceleration region  $\xi < 0$ . This case corresponds to a Reynolds number of  $Re_{\text{Sumer}} = 6 \cdot 10^7$ , which is more than an order of magnitude larger than the result by Sumer et al. (2010).

We found that for all values of  $\epsilon$  and  $\delta$  considered the boundary layer flow displays regions of growth of instabilities, confirming the results by Blondeaux et al. (2012). As also mentioned by Blondeaux et al. (2012), this is, however, in contrast to the apparent findings by Sumer et al. (2010) and Vittori and Blon-

deaux (2008, 2011) which state that below a critical Reynolds number  $Re_{\text{Sumer}}$ , the boundary layer profile does not depart from its shape given by the boundary layer equations (29-31). At the critical Reynolds number the references reported, the boundary layer flow performs a transition from the solution given by the boundary layer equations (29-31) to a laminar flow with periodic vortex shedding. This critical Reynolds number has been determined by Sumer et al. (2010) to have the value  $Re_{\text{Sumer}} = 2 \cdot 10^5$ , whereas Vittori and Blondeaux (2011) put this value higher, somewhat below  $Re_{\text{Sumer}} = 5 \cdot 10^5$ , cf. figure 5 in Vittori and Blondeaux (2011). As reported, a second transition from laminar vortex shading to turbulent flow arises for higher values of  $Re_{\text{Sumer}}$ . In the present discussion, we focus on the first transition where the boundary layer flow solution, given by equation (29-31), becomes unstable. We do, however, not make any prediction on what will happen after transition. Linear stability cannot predict what happens once the flow turns unstable. The flow might become turbulent, it might go over to a different laminar regime or as we shall see it might also continue to 'display' the original solution given by the boundary layer equations (29-31).

Since, in the sense of linear stability the flow is always unstable, the question is rather when do these instabilities become visible. Blondeaux et al. (2012) tried to answer this question by looking at the kinetic energy of the perturbations in their Navier-Stokes solution. They observed that when fixing  $\delta$  the growth of the kinetic energy of the perturbations becomes more important for increasing  $\epsilon$  until for a critical  $\epsilon_c$ , the kinetic energy of the perturbations cannot be neglected anymore. They therefore concluded that a critical set of parameters  $(\delta_c, \epsilon_c)$  can be given for which the flow turns unstable, although they admit that there is a certain arbitrariness in the choice of  $(\delta_c, \epsilon_c)$ . Their analysis is, however, misleading. As we shall see, the fact when a flow turns visibly unstable depends in a great deal on the initial amplitude of the perturbation which was uncontrolled in the experiments by Sumer et al. (2010) and also in the simulations by Vittori and Blondeaux (2008, 2011). Visibility of the instability can be measured by the amplification of the perturbation. As a matter of fact a general perturbation consists of all possible frequencies  $\omega$  and the amplification of each mode should be investigated. To simplify the analysis we only consider the amplification of a Tollmien-Schlichting wave of frequency  $\omega_c$  where  $\omega_c$  is the frequency of the Tollmien-Schlichting starting to grow at the critical position  $\xi_c$ . The parameter range investigated is  $\delta = 8 \cdot 10^{-4}$  and  $\epsilon = 0.1, 0.2, 0.3, 0.4$ . The stability domains for these cases have been displayed in figure 14 and by going along the neutral curve to its leftmost extremum, the critical position  $\xi_c$  can be found. The critical parameters for the Tollmien-Schlichting waves have been listed in table 1. The cases  $\delta = 8 \cdot 10^{-4}$  and  $\epsilon = 0.1, 0.2, 0.3, 0.4$  have also been investigated by Vittori and Blondeaux (2008, 2011). In figure 1 in Vittori and Blondeaux (2011), time profiles of the horizontal velocity component at a point in space are plotted. In addition, in figure 5 in Vittori and Blondeaux (2011) it is clearly visible that the case  $(\epsilon = 0.1, \delta = 8 \cdot 10^{-4})$  has been considered stable by both Sumer et al. (2010) and Vittori and Blondeaux (2011). The cases  $(\epsilon = 0.3, \delta = 8 \cdot 10^{-4})$  and  $(\epsilon = 0.4, \delta = 8 \cdot 10^{-4})$  on the other hand were found



to be unstable by both Sumer et al. (2010) and Vittori and Blondeaux (2011). However, the case ( $\epsilon = 0.2, \delta = 8 \cdot 10^{-4}$ ) was classified unstable by Sumer et al. (2010), whereas Vittori and Blondeaux (2011) deemed it stable.

In figure 22 the growth of the Tollmien-Schlichting wave has been recorded in terms of the amplification of the perturbation, cf. equation (55), using the parabolic stability equation solver. At the chosen point  $\xi = 19.5$ , we measured the amplitude of the signal and compared it with the minimum amplitude at the critical position  $\xi_c$ , of the signal which gives us the amplification of the signal at the above point. These amplifications are listed in table 1. The value  $\xi = 19.5$  seemed reasonable to us, since the maximum extension in time behind the crest used by Vittori and Blondeaux (2011) for example in figure 1 in Vittori and Blondeaux (2011) is 20 which corresponds approximately to a spatial extension between 21 and 23.6. If we assume for the time being that the Tollmien-Schlichting waves start to roll up into vortices once their amplitude has grown to a value comparable to the mean flow, of order 1 thus, we obtain the result that the initial perturbation at  $\xi_c$  for the case ( $\epsilon = 0.1, \delta = 8 \cdot 10^{-4}$ ) has at least been smaller than  $10^{-2.7}$  in the experiments by Sumer et al. (2010) and the simulations by Vittori and Blondeaux (2008, 2011). The case ( $\epsilon = 0.3, \delta = 8 \cdot 10^{-4}$ ) on the other hand tells us that the perturbation for both Sumer et al. (2010) and Vittori and Blondeaux (2008, 2011) must have had an initial amplitude approximately equal or larger than  $10^{-6.5}$ . Since the experiments turned unstable for  $\epsilon = 0.2$ , the initial amplitude in the experiments must have been approximately equal or larger than  $10^{-5}$ . On the other hand the amplitude of the perturbation at the critical position in the simulations by Vittori and Blondeaux (2008, 2011) must have been smaller than  $10^{-5}$  for this case. In figure 1(b) in Vittori and Blondeaux (2011) some wiggles in the temporal evolution of the horizontal velocity appear at approximately  $t = 6$  behind the crest for the case ( $\epsilon = 0.3, \delta = 8 \cdot 10^{-4}$ ), using the speed  $c$  of a solitary wave for this amplitude, this point in time corresponds to a position behind the crest of  $\xi = 6.83$ . From figure 22, we obtain an amplification of  $10^{5.0}$  at  $\xi = 6.83$ . The same can be done for the case ( $\epsilon = 0.4, \delta = 8 \cdot 10^{-4}$ ), cf. figure 1(c) in Vittori and Blondeaux (2011), where the wiggles start at approximately  $t = 4$  behind the crest, corresponding to  $\xi = 4.71$ . The amplification at that position, taken from figure 22 is  $10^{4.7}$ . Although the above analysis is relatively crude, since the works by Sumer et al. (2010), by Vittori and Blondeaux (2008, 2011) and the present one are not comparable in detail, it suggests that at the critical position  $\xi_c$  the amplitude of the perturbation in the simulations by Vittori and Blondeaux (2008, 2011) was smaller than that of the perturbation in the experiments by Sumer et al. (2010). Since linear stability predicts a strong decay of the perturbations in the acceleration region, the initial  $10^{-4}$  amplitude perturbation, which Vittori and Blondeaux (2008, 2011) reported to have imposed onto the initial condition before the solitary wave arrived, should have decayed until the critical position to values much lower than the  $10^{-5}$  estimated above. In addition, since they introduced white noise the initial amplitude on a Tollmien-Schlichting wave, conceivable as the result of a normal mode decomposition, would be much less than  $10^{-4}$ . According to this, combined with our analysis, they should not have

observed appreciable instabilities for the case in question ( $\epsilon = 0.3, \delta = 8 \cdot 10^{-4}$ ). Unfortunately, no sensitivity test on the influence of the initial perturbation was reported in Vittori and Blondeaux (2008, 2011) and Blondeaux et al. (2012). It would be of interest how their results would change from the published once, if, for instance, no initial seeding or seeding with a certain spectrum had been applied. However, the Navier-Stokes solver used in Vittori and Blondeaux (2008, 2011) and Blondeaux et al. (2012) may have produced a certain level of numerical noise, which might have provided a sufficient level at  $\xi_c$  for instabilities to become visible. We find support for this presumption in figure 4 in Blondeaux et al. (2012), where the level of kinetic energy of the perturbation seems to stay on a stable level of around  $10^{-8} - 10^{-9}$  for all cases of  $\epsilon$ , before arriving at the critical position. This indicates that their code bears a source of numerical noise with an amplitude of approximately  $10^{-4} - 10^{-4.5}$ , which combined with an amplification factor of  $10^5$ , as found above, well may have caused visible disturbances. Several reasons for the numerical source of noise are thinkable, such as truncation errors or incomplete pressure solutions. As a conclusion, it needs to be said that in the works of Sumer et al. (2010), Vittori and Blondeaux (2008, 2011) and Blondeaux et al. (2012), the triggering mechanism of the instability is not well controlled. Since the initial amplitude is crucial for the visual appearance of the perturbation, the meaning of classifications such as the one presented in figure 5 in Sumer et al. (2010) or figure 5 in Vittori and Blondeaux (2011) or the determination of critical parameters ( $\delta_c, \epsilon_c$ ) in Blondeaux et al. (2012) needs to be taken with care. A boundary layer flow under a solitary wave considered to be unstable by criteria proposed by either Sumer et al. (2010), Vittori and Blondeaux (2008, 2011) or Blondeaux et al. (2012), might in a different setting seem to be stable as long as the initial amplitude of the perturbation at the critical position is smaller than its amplification. On the other hand, a flow determined to be stable by one of the above criteria might display instabilities once the initial amplitude is equal or larger than its amplification. In their related study on boundary layers on a  $10^\circ$  beach Pedersen et al. (2013) reported (section IVA) for one case (incident wave with  $\epsilon = 0.3$ ) that instability occurred in an up-beach position, immediately after an inflection point in the boundary layer profile was observed. However, this was observed in 3 out of 4 experiments, and never in a location close to equilibrium shoreline, where inflection points in the retardation phase were also present. In view of the present investigation we presume that the flow in those experiments were unstable in most of the retardation phase and that the visible appearance of instabilities was due to the integrated amplification factor and the level of disturbances, which in this case may stem from particle seeding (for PIV measurements), contact point dynamics and residual motion from preceding experiment. In fact, unless the disturbances are actively controlled we do not believe that experimental repeatability for a flow transition of this type can be obtained.

A quantity of interest, also investigated in Blondeaux et al. (2012), is the phase speed of the critical Tollmien-Schlichting wave. For a given frequency  $\omega$ , the wavenumber of the Tollmien-Schlichting wave can approximately be given by  $\text{Im}(a)$ , where  $a$  is defined in equation (47). In figure 23, the phase speed in the

Table 1: Critical parameters for the case  $\delta = 8 \cdot 10^{-4}$ , for different values of  $\epsilon$

$\epsilon$	$c$	$\xi_c$	$t_c = \xi_c/c$	$\omega_c$	$k_c$	$A(\xi = 19.5)/A_{\min}$
0.1	1.049	2.125	2.03	0.218	0.212	$10^{2.7}$
0.2	1.094	1.249	1.14	0.228	0.218	$10^{5.0}$
0.3	1.138	0.969	0.85	0.230	0.216	$10^{6.5}$
0.4	1.179	0.820	0.70	0.240	0.220	$10^{7.5}$

absolute frame of reference for the critical Tollmien-Schlichting waves is plotted as a function of  $\xi$ . The parameters for the plotted cases are given in table 1. The Tollmien-Schlichting waves seem to first propagate in the direction of the solitary wave and then reverse their direction of propagation. This result has also been obtained by Blondeaux et al. (2012) for their perturbations. They proposed that the flow reversal in the boundary layer is causing the Tollmien-Schlichting waves to reverse their direction of propagation too. From figure 23, we observe that for increasing amplitudes  $\epsilon$ , the Tollmien-Schlichting waves travel with an increasing phase speed. The reason may be that the magnitude of the particle velocities in the base flow become higher for increasing  $\epsilon$ .

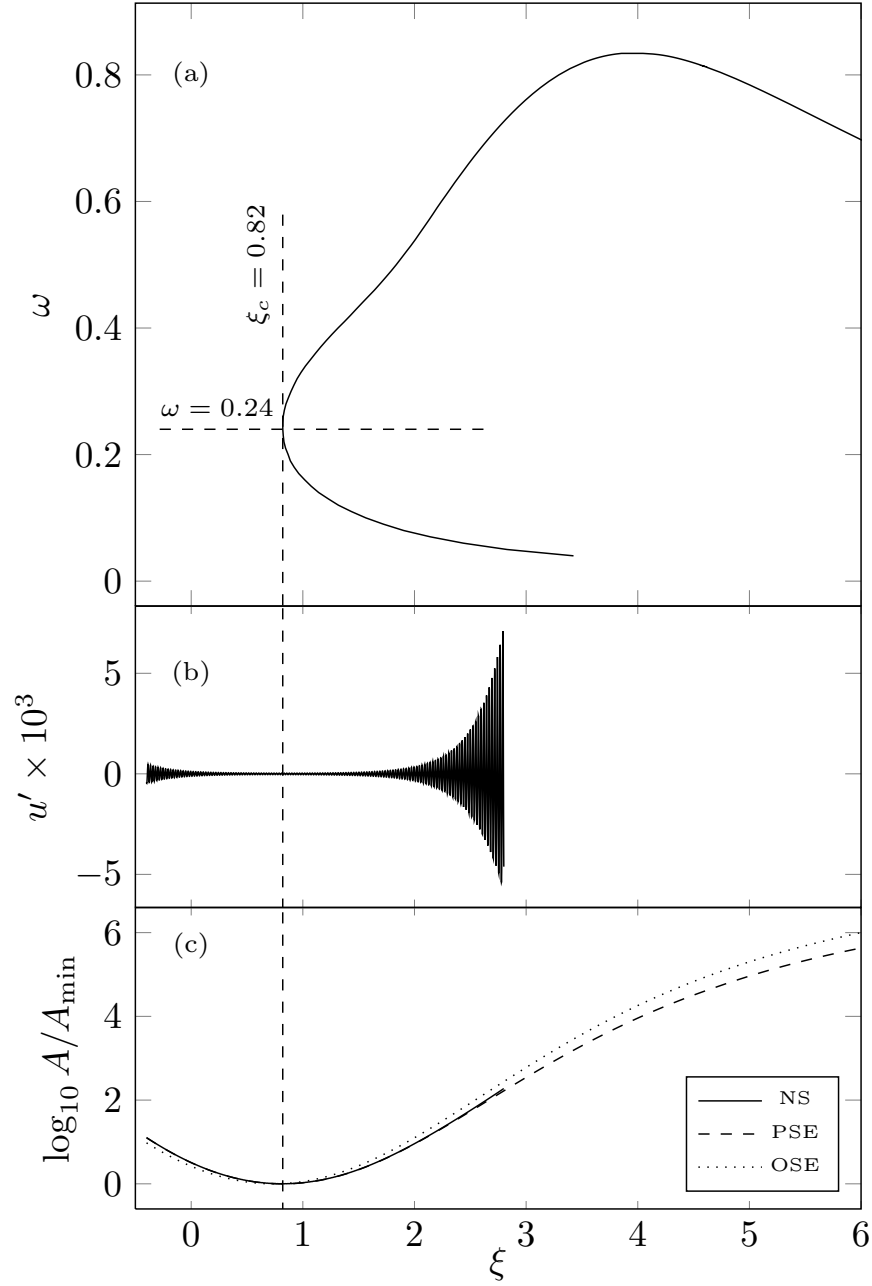


Figure 10: (a) Stability domain for the case  $\epsilon = 0.4$  and  $\delta = 8 \cdot 10^{-4}$ . (b) Horizontal perturbation  $u'$  of the horizontal velocity component recorded at a distance  $y = 0.4943$  from the wall for a Tollmien-Schlichting wave of  $\omega = 0.24$  computed by means of the Navier-Stokes solver. (c) Amplification of the Tollmien-Schlichting wave with  $\omega = 0.24$  computed by means of the Orr-Sommerfeld equation solver (OSE), the parabolic stability equation solver (PSE) and the Navier-Stokes solver (NS). Here and in the subsequent figures:  $\xi$  is scaled by (15), while  $\omega$  by means of (16).

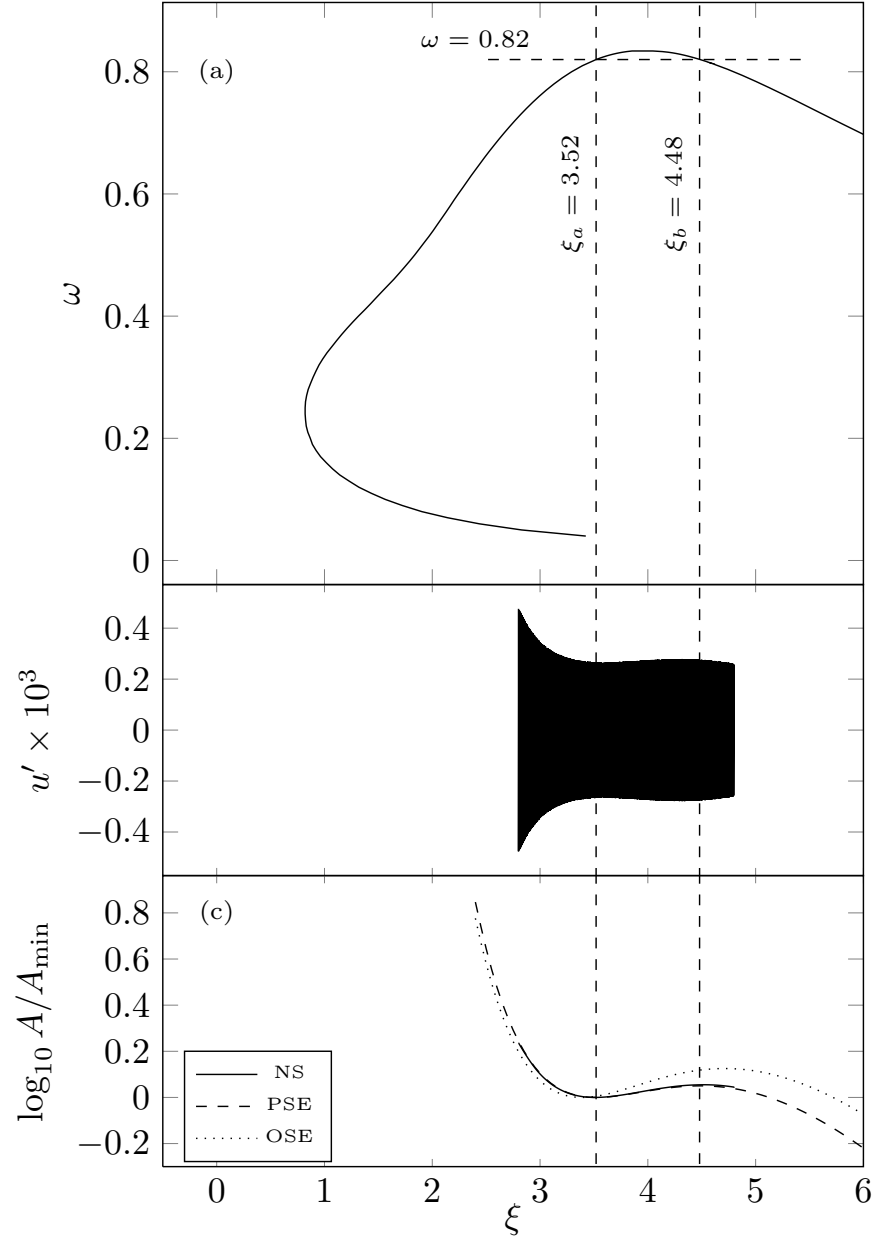


Figure 11: (a) Stability domain for the case  $\epsilon = 0.4$  and  $\delta = 8 \cdot 10^{-4}$ . (b) Horizontal perturbation  $u'$  of the horizontal velocity component recorded at a distance  $y = 0.4943$  from the wall for a Tollmien-Schlichting wave of  $\omega = 0.82$  computed by means of the Navier-Stokes solver. (c) Amplification of the Tollmien-Schlichting wave with  $\omega = 0.82$  computed by means of the Orr-Sommerfeld equation solver (OSE), the parabolic stability equation solver (PSE) and the Navier-Stokes solver (NS).

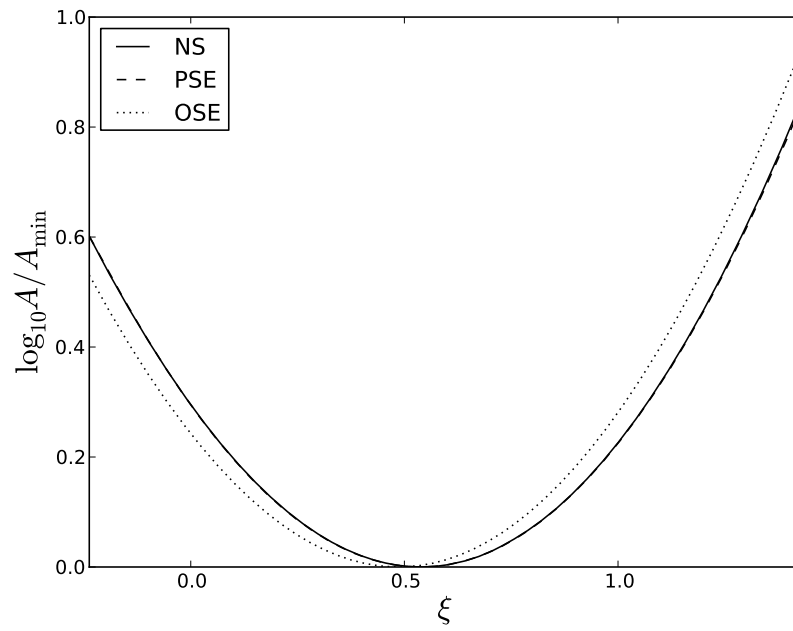


Figure 12: Amplification of the Tollmien-Schlichting wave for the case  $\epsilon = 0.4$ ,  $\delta = 4.75 \cdot 10^{-4}$  and  $\omega = 0.22$ . The amplification has been computed by means of the Orr-Sommerfeld equation solver (OSE), the parabolic stability equation solver (PSE) and the Navier-Stokes solver (NS).

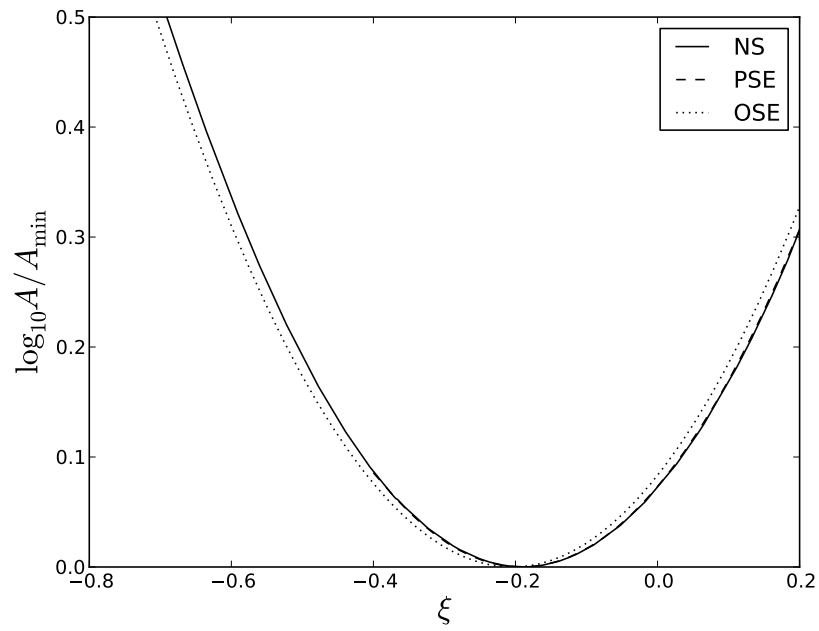


Figure 13: Amplification of the Tollmien-Schlichting wave for the case  $\epsilon = 0.4$ ,  $\delta = 10^{-4}$  and  $\omega = 0.185$ . The amplification has been computed by means of the Orr-Sommerfeld equation solver (OSE), the parabolic stability equation solver (PSE) and the Navier-Stokes solver (NS).

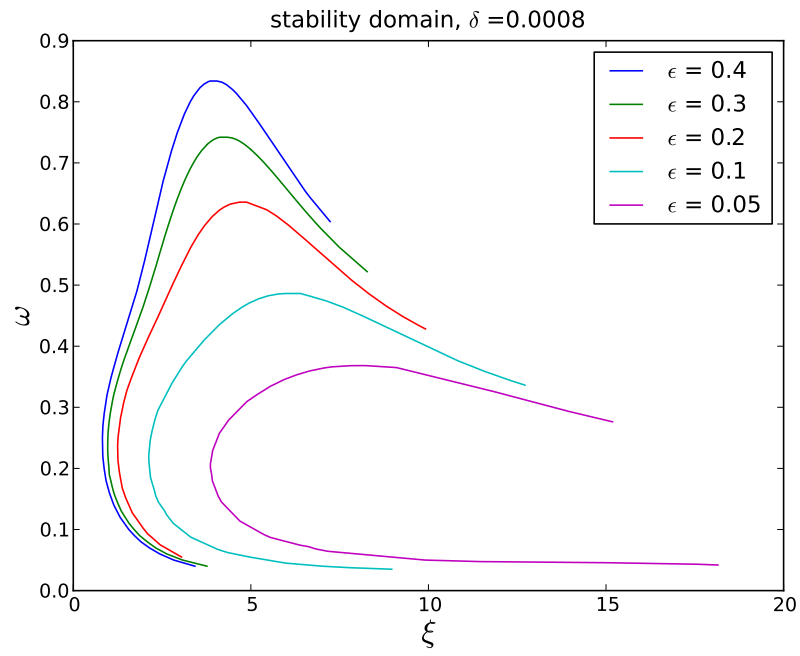


Figure 14: Stability domain for  $\delta = 8 \times 10^{-4}$ . The region bounded by the curves is the unstable region.



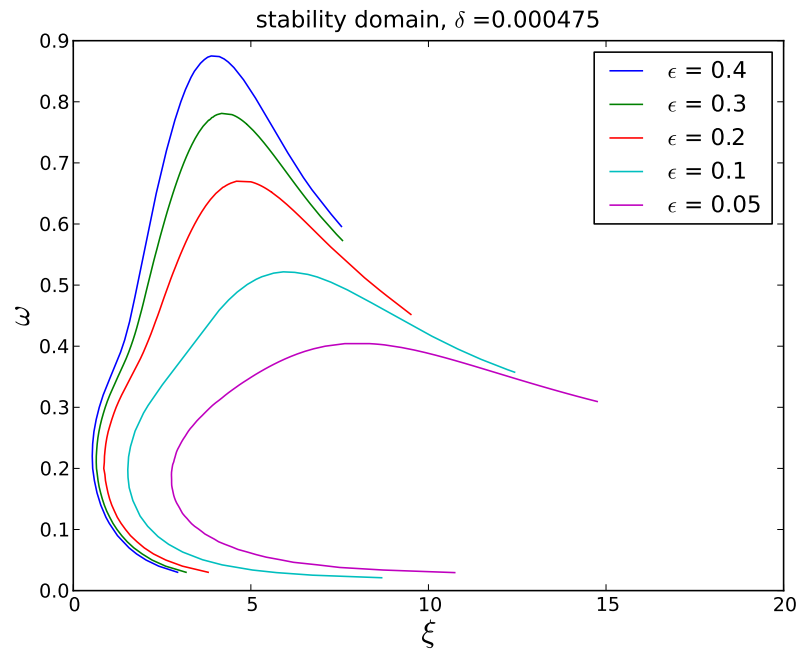


Figure 15: Stability domain for  $\delta = 4.75 \times 10^{-4}$ . The region bounded by the curves is the unstable region.

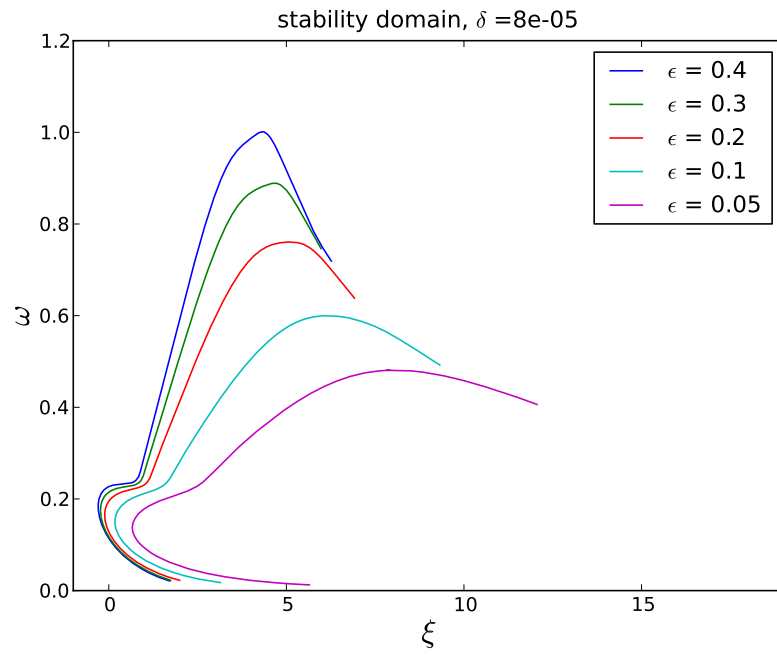


Figure 16: Stability domain for  $\delta = 8 \times 10^{-5}$ . The region bounded by the curves is the unstable region.

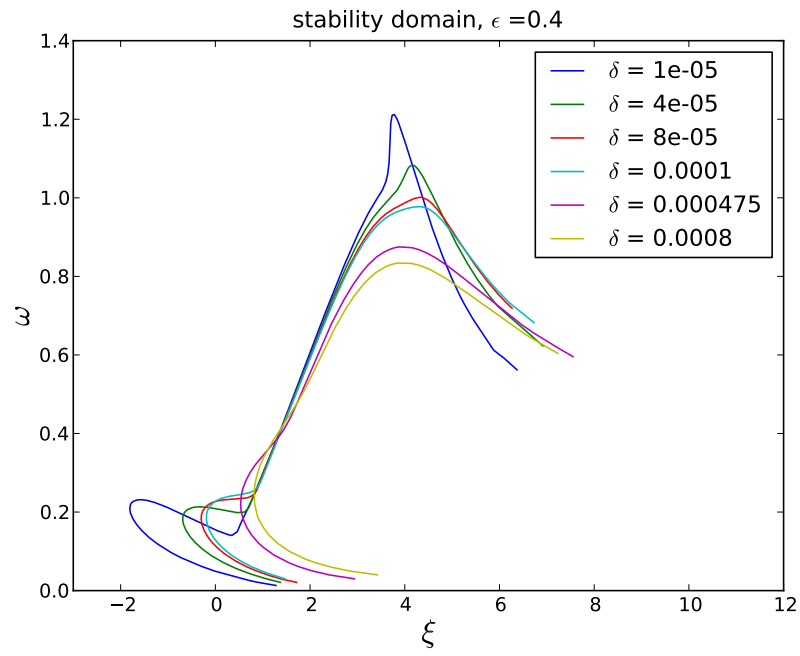


Figure 17: Stability domain for  $\epsilon = 0.4$ . The region bounded by the curves is the unstable region.

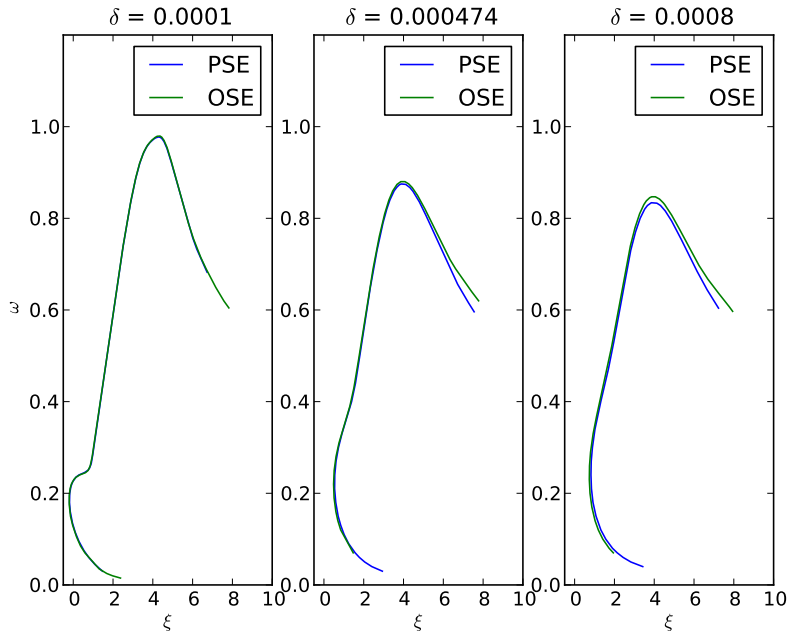


Figure 18: Comparison of the unstable region for the cases  $\epsilon = 0.4$  and  $\delta = 8 \cdot 10^{-4}, 4.75 \cdot 10^{-4}, 10^{-4}$  computed by means of the Orr-Sommerfeld equation (OSE) and the parabolic stability equation (PSE).

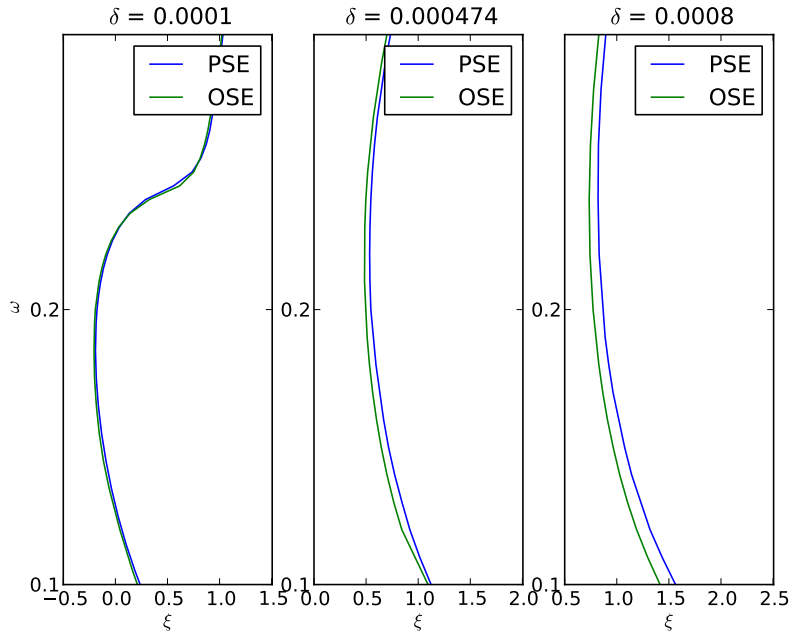


Figure 19: Zoom onto parts of the unstable regions displayed in figure 18.

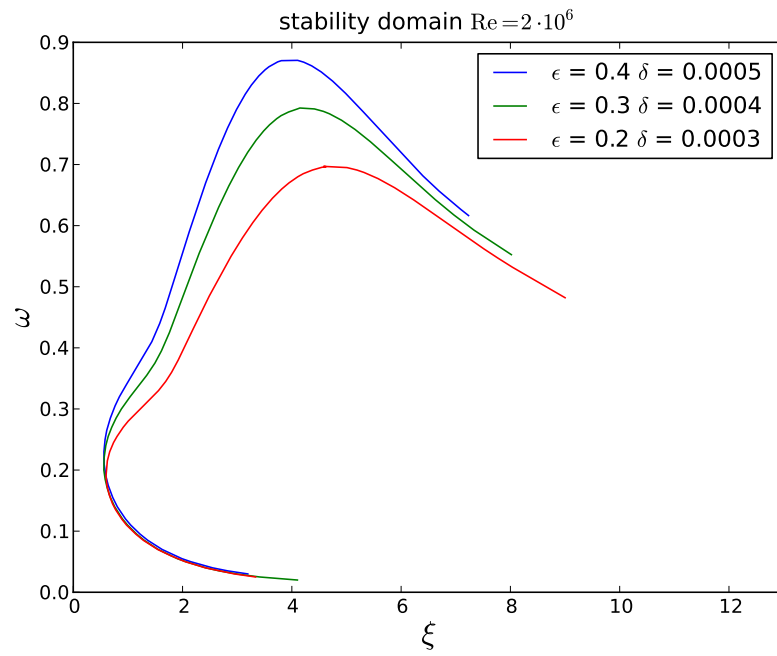


Figure 20: Stability domain for  $Re_{\text{Sumer}} = 2 \cdot 10^6$ . The amplitude  $\epsilon$  and the parameter  $\delta$  are chosen in such a way that  $Re_{\text{Sumer}}$  is approximately equal to  $2 \cdot 10^6$ .

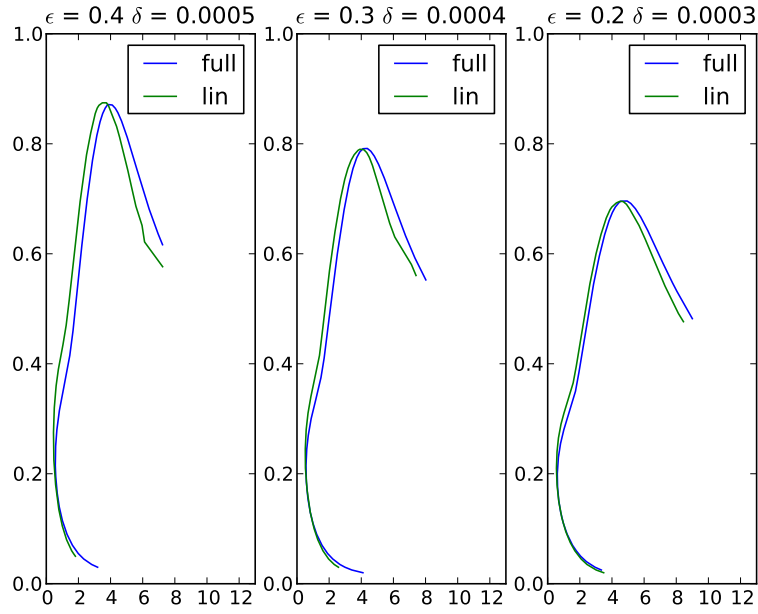


Figure 21: Stability domains for the linearized boundary layer profile by Liu et al. (2007) and the nonlinear profile based on the full potential solution, for  $Re_{\text{Summer}} = 2 \cdot 10^6$ . The amplitude  $\epsilon$  and the parameter  $\delta$  are chosen in such a way that  $Re_{\text{Summer}}$  is approximately equal to  $2 \cdot 10^6$ .

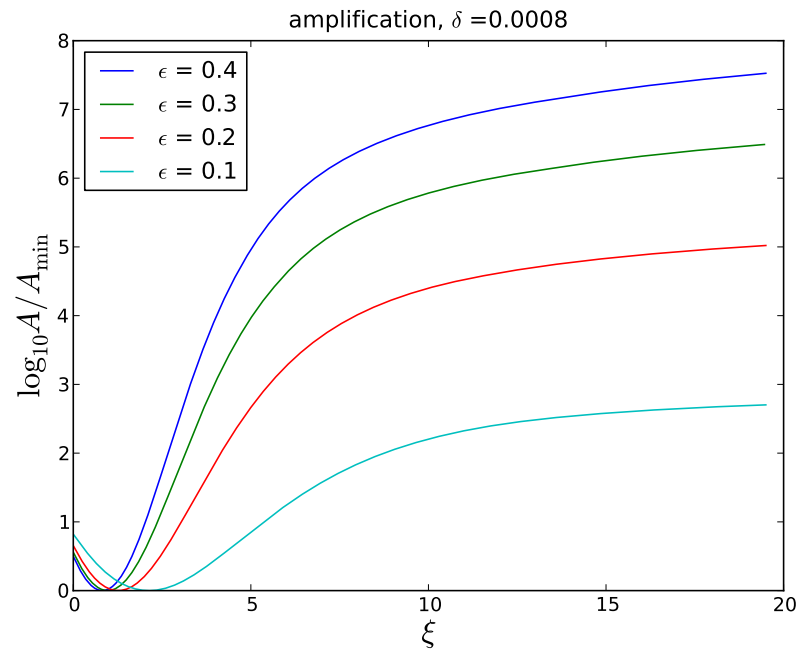


Figure 22: Amplification of Tollmien-Schlichting waves for the cases listed in table 1 using the parabolic stability equation solver.



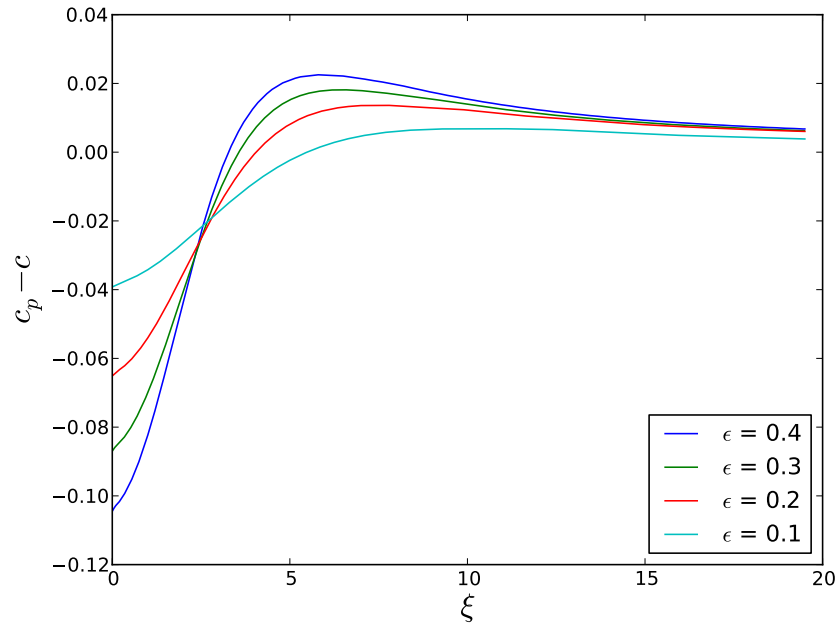


Figure 23: Absolute phase speed  $c_p - c$  of Tollmien-Schlichting waves for  $\delta = 8 \cdot 10^{-4}$ . The parameters of the Tollmien-Schlichting waves are given in table 1.

## 5 Conclusions

In the present treatise, the nonlinear solution of the boundary layer under a solitary wave is computed. Unlike Liu et al. (2007) we find that the linear and nonlinear profiles differ significantly for increasing amplitude  $\epsilon$  of the solitary wave. Consequently, our further analysis is based on a fully nonlinear boundary layer theory, unlike the preceding studies from the literature. The stability of the boundary layer flow is investigated by means of two methods based on model equations, the Orr-Sommerfeld equation and the parabolic stability equation, and a direct numerical simulation by a spectral Navier-Stokes solver. We confirmed the result by Blondeaux et al. (2012) that in the sense of linear stability, the boundary layer flow is always unstable for the parameter range considered, meaning that Tollmien-Schlichting waves will start to grow once they reach the critical position  $\xi_c$ . This critical position can be obtained by computing the stability domains for different amplitudes  $\epsilon$  of the solitary wave and different viscosity parameters  $\delta$ , which is inversely proportional to the Reynolds number. Increasing  $\epsilon$  or decreasing  $\delta$  will increase the unstable region of the flow. By comparing the stability domain by the linear solution by Liu et al. (2007) to the one of the present nonlinear solution, we found that perturbations start to grow earlier (smaller  $\xi_c$ ) in the linear case and that the critical frequency is higher than in the nonlinear case. Using the Orr-Sommerfeld equation and the parabolic stability equation, the nonparallel effects of the flow were analyzed. For small  $\delta$  the nonparallel effects become less significant. However, for larger values of  $\delta$ , they will retard the critical position. For low values of  $\epsilon$  and/or high values of  $\delta$ , the unstable region is in the deceleration region of the wave, where the pressure gradient is favorable to instability. However, decreasing  $\delta$  sufficiently will lead to the growth of a 'tongue' shaped region extending into the acceleration region of the flow, which is by Rayleigh's inflection point theorem a stable region for inviscid flow. Therefore viscosity plays a major role for this instability. Although only qualitatively, this supports the observation of instabilities in the acceleration region by Sumer et al. (2010) in their experiments. We underline, however, that such instabilities may only be found for water depths larger than those used in normal wave tank experiments. Vittori and Blondeaux (2008, 2011) did not observe instabilities before the crest, since the Reynolds numbers they considered were too small. However, opposed to the present results, Sumer et al. (2010) by means of experiments and Vittori and Blondeaux (2008, 2011) by means of simulations found that the flow turns unstable only beyond a certain critical Reynolds number  $Re_{\text{Sumer}}$ , which differed for the experiments and the simulations. Similar Blondeaux et al. (2012) postulated that a critical set of parameters  $(\epsilon, \delta)$  can be defined for this flow. By looking at the amplification of the perturbation it was shown herein that not only differences in the base flow field but also the initial amplitude of the perturbation might be the reason why for the experiments by Sumer et al. (2010) the flow turned unstable for one Reynolds number whereas it did not for the simulations by Vittori and Blondeaux (2008, 2011). As such we found that a critical Reynolds number or a critical set of parameters  $(\epsilon, \delta)$  for this flow does not exist and that

we at most might give a criterion dependent on the initial amplitude of the perturbation for the appearance of transition in the flow field. A possible direction for future research is investigation of the boundary layer flow under a solitary wave by means of nonlinear stability analysis where Tollmien-Schlichting waves with different frequencies interact with each other. In addition, the roll up of the Tollmien-Schlichting waves into vortices in connection with the initial seeding of the perturbation needs to be investigated more in detail. This topic touches also the appearance of turbulent spots observed by Sumer et al. (2010) leading to the question of how the growth of Tollmien-Schlichting waves, the roll up into vortices and the interaction with turbulent spots produce transitions in the boundary layer under a solitary wave.

Prof. Arnold Bertelsen is cordially acknowledged for interesting discussions. The work was supported by the Norwegian Research Council under the project 205184/F20.

The computations were partly performed on the Abel Cluster, owned by the University of Oslo and the Norwegian metacenter for High Performance Computing (NOTUR).

## A Verification and validation of the boundary layer solver

The verification of the boundary layer solver, derived in subsection 3.1, was done by means of a manufactured solution, cf. subsection A.1. We validated the method by applying it to the Blasius boundary layer problem, for which an accurate reference solution exists, cf. subsection A.2. Finally in subsection A.3, we investigated the convergence of the method, when applied to the problem of the boundary layer under a solitary wave.

### A.1 Verification by means of a toy problem

In order to verify the boundary layer equations solver proposed in subsection 3.1, we used the artificial field

$$u^{\text{ref}} = -y^{n-1} \cos x \quad v^{\text{ref}} = \frac{1}{n} y^n \sin x, \quad (101)$$

which satisfies the continuity equation (29) with an external pressure gradient given by

$$-\frac{\partial p^{\text{ext}}}{\partial y} = u^{\text{ref}} \frac{\partial u^{\text{ref}}}{\partial x} + v^{\text{ref}} \frac{\partial u^{\text{ref}}}{\partial y} - \frac{1}{2} \frac{\partial^2 u^{\text{ref}}}{\partial y^2}. \quad (102)$$

This pressure gradient should reproduce the velocity field (101). We remark that the external pressure gradient (102) does not satisfy equation (31). This does, however, not represent a flaw for verifying the boundary layer solver derived in subsection 3.1. Figure 24 shows the convergence of the method for this problem, when choosing  $n = 4$ . For this simple problem we observe spectral convergence

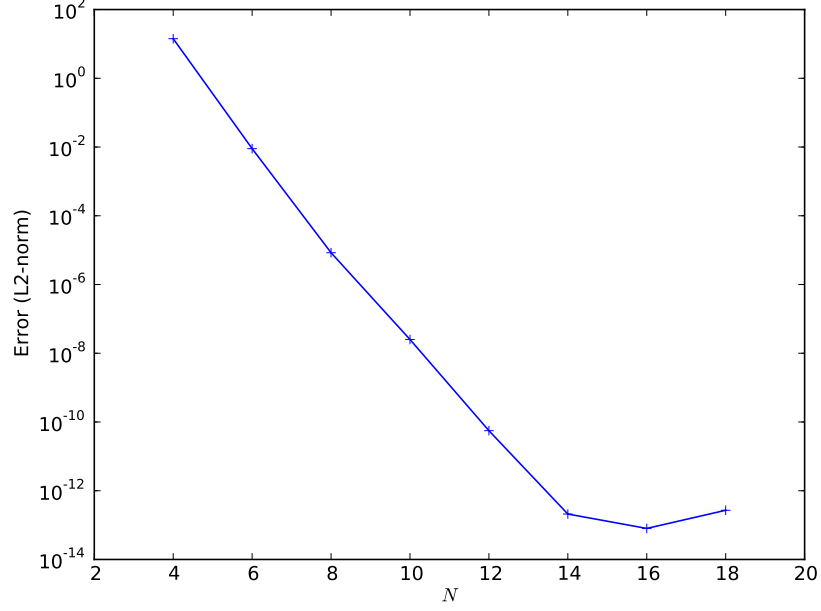


Figure 24: Convergence of the boundary layer solver described in subsection 3.1 for the toy problem 101

of the method. The round off accuracy is already obtained with only  $N_{BL} = 14$ . The error was measured in the  $L2$  norm.

## A.2 Validation by means of the Blasius boundary layer flow

For the Blasius boundary layer problem Ryhming (2004) a well known numerical solution exists. In order to validate the boundary layer solver in subsection 3.1, we applied the present scheme to solve the boundary layer equations for a flat plate. The result was then compared to the Blasius boundary layer solution by means of the  $L2$  norm. The domain of integration was from  $Re_x = 100$  to  $Re_x = 200$ . The convergence of the method for increasing  $N_{BL}$  can be observed in figure 25. The error decreases spectrally up to a value of  $10^{-10}$  after which it stagnates. The reason for this might be the accumulation of round off error or due to some coarse internal parameters in the inbuilt ordinary differential equation solver by MATLAB used to generate the reference solution.

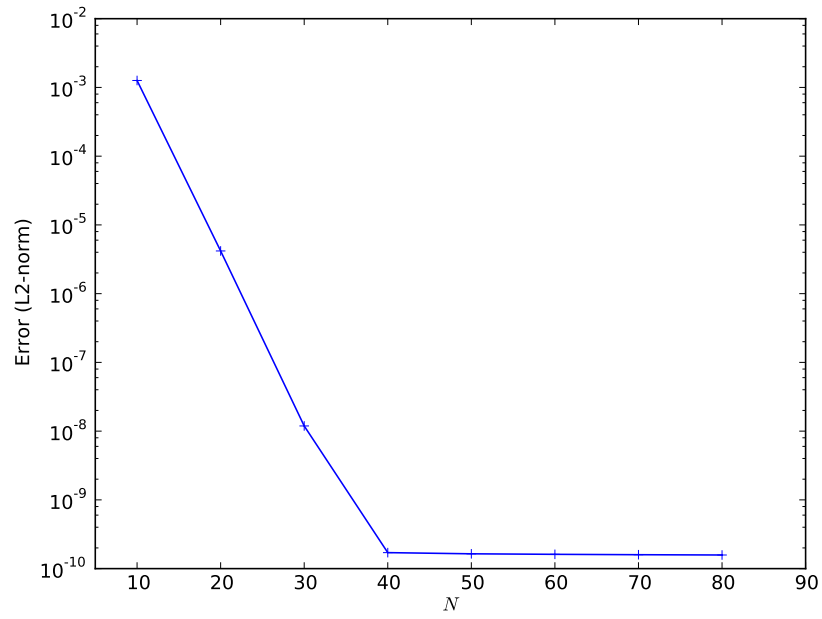


Figure 25: Convergence of the boundary layer solver described in subsection 3.1 for the Blasius boundary layer.

### A.3 Validation by means of the boundary layer flow under a solitary wave

As a last benchmark test, we tested the convergence of the boundary layer solver, cf. subsection 3.1, for the boundary layer flow under a solitary wave itself, in particular for the parameter  $\epsilon = 0.4$  and for different domain sizes given by  $y^{\text{ext}}$  and  $L_x$ . The reference solutions have in this case been produced by using the boundary layer solver on a fine grid with  $N_{\text{BL}} = 80$ . The results can be seen in figure 26. The convergence appears to be only spectral for a resolution up to  $N_{\text{BL}} \approx 40$  for the larger domain sizes, after which the error oscillates around  $10^{-4}$ . Increasing the resolution of the reference solution did not lead to better results. The reason for this behavior is that the inviscid flow solution is only accurate up to  $10^{-4}$ . This can also be seen by the fact that for smaller domains the convergence is better until we reach a level of the error of approximately  $10^{-4}$  behind which the convergence stagnates, cf figure 26, since the inviscid flow is the same for all domain sizes. For a smaller value of  $\epsilon$ , namely  $\epsilon = 0.2$  ( $y^{\text{ext}} = 20$  and  $L_x = 20$ ), the accuracy is somewhat better. In order to be on the safe side concerning the accuracy of the numerical solution for different values of  $\epsilon$ , we chose a value of  $N_{\text{BL}} = 80$  for all simulations in section 4. The domain size parameters are chosen  $y^{\text{ext}} = 60$  and  $L_x = 20$  such that the domain is large enough in order to accommodate the full width of the Tollmien-Schlichting waves. This way the numerical solution to the boundary layer equations (29-30) can be assumed to be accurate up to the fourth digit.

## B Verification and validation of the Orr-Sommerfeld solver

As for the boundary layer solver, we verified and validated the present Orr-Sommerfeld solver derived in subsection 3.2 by means of the Blasius boundary layer and by means of the boundary layer under solitary wave itself.

### B.1 Verification and validation by means of the Blasius boundary layer

Jordinson (1970) was the first to use the Orr-Sommerfeld equation to investigate spatial instabilities of the Blasius boundary layer. He presented the values for  $a$ , equation (42),

for a few selected cases. We computed the eigenvalues for these cases, which are listed below. These results are obtained by using  $N_{\text{OSE}} = 80$  and  $N_{\text{OSE}} = 120$ . Only the coinciding digits of the solutions have been printed. All results are given in the scaling used in Jordinson (1970) and can be compared with the values given therein.

- Case 1:  $Re = 336$ ,  $\omega = 0.1297$

$$a = -0.007952136 + 0.308318511i$$

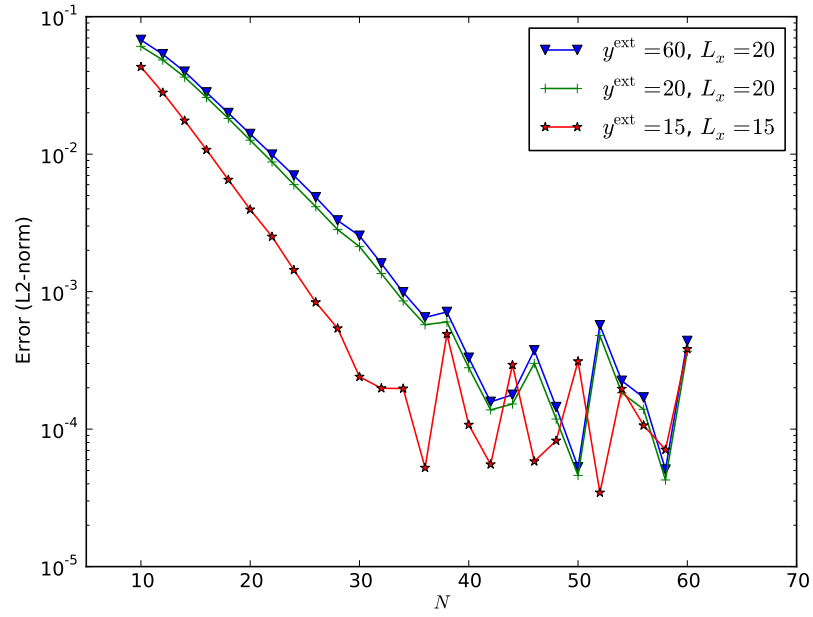


Figure 26: Convergence of the boundary layer solver described in subsection 3.1 for the boundary layer under a solitary wave with  $\epsilon = 0.4$ .

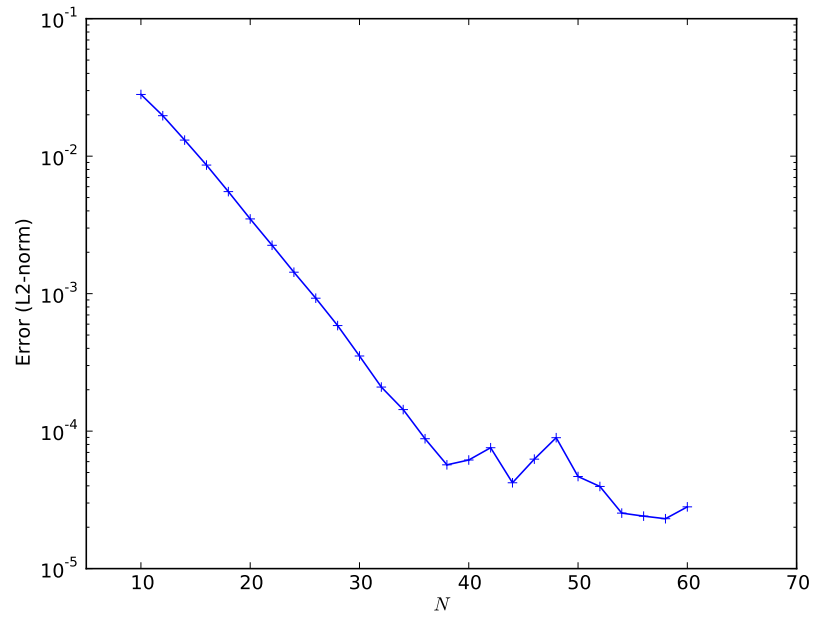


Figure 27: Convergence of the boundary layer solver described in subsection 3.1 for the boundary layer under a solitary wave with  $\epsilon = 0.2$ .



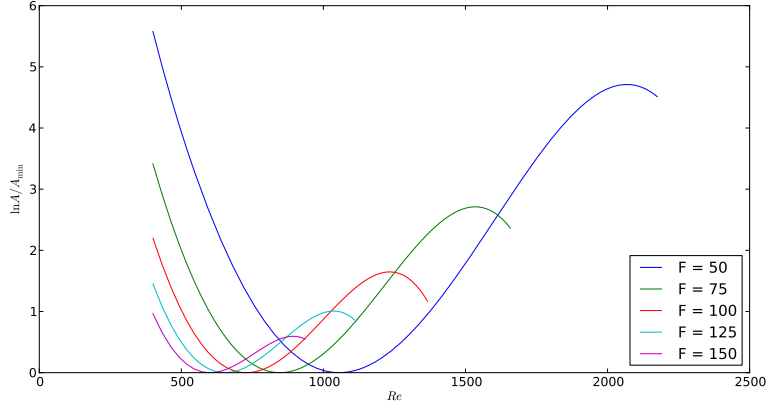


Figure 28: Amplification curves for the Blasius boundary layer using the Orr-Sommerfeld solver, cf. subsection 3.2, for different frequencies  $F \times 10^6 = 50, 75, 100, 125, 150$ . The results can be compared to the results in figure 4(a) in Jordinson (1970).

- Case 2:  $Re = 598$ ,  $\omega = 0.1201$

$$a = 0.001893765 + 0.307831329i$$

- Case 3:  $Re = 998$ ,  $\omega = 0.1122$

$$a = 0.005707382 + 0.308584442i$$

By comparing the above values to the values given in Jordinson (1970), we see that some of the above growth rates and wave numbers display small differences on the fourth decimal. In addition, we computed the amplifications for the frequencies  $F \times 10^6 = 50, 75, 100, 125, 150$ , cf. figure 28. For the precise definition of  $F$ , we refer to Jordinson (1970). When comparing the present results to the corresponding results in Jordinson (1970), figure 4(a) therein, we see that the amplification for lower frequencies seems to coincide well. However, for higher frequencies the present amplifications reach their maximum earlier than in Jordinson (1970). We accord this difference to the different numerical methods used in Jordinson (1970) and in the present work. We remark that the graphs in figure 28 were obtained by using two resolutions  $N_{BL} = 80$  and  $N_{BL} = 120$  giving results identical to plotting accuracy.

## B.2 Validation by means of the boundary layer under a solitary wave

In order to determine the resolution  $N_{OSE}$  necessary to obtain meaningful results, we used the present Orr-Sommerfeld solver to compute the stability do-

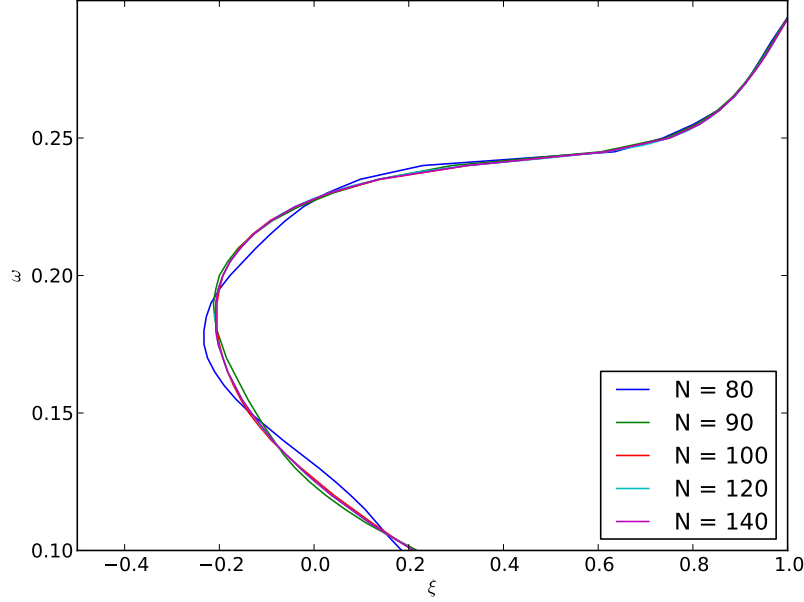


Figure 29: The stability domain for the case  $\epsilon = 0.4$  and  $\delta = 10^{-4}$  computed using the Orr-Sommerfeld solver derived in subsection 3.2 for different resolution  $N_{\text{OSE}}$ .

main for the case  $\epsilon = 0.4$  and  $\delta = 10^{-4}$  for different resolutions. A zoom onto the neutral curve can be seen in figure 29. For resolutions  $N_{\text{OSE}} \geq 100$  the curves are almost identical. For finer resolutions, the neutral curve oscillates around the curve of finer resolution. These oscillations become smaller and smaller in amplitude and osculate to the limiting curve. The accuracy chosen for all simulations using the Orr-Sommerfeld solver in section 4 was  $N_{\text{OSE}} = 130$ . This was done in order to keep the error contribution by the Orr-Sommerfeld solver subdominant comparing to the error contribution by the potential solver.

## C Verification and validation of the parabolic stability equation solver

The parabolic stability equation solver, derived in subsection 3.3 was verified the same way as the Orr-Sommerfeld equation solver. First, we used data in the literature to verify the correct implementation of the method by means of the Blasius boundary layer. After that we investigated the convergence of the method when applied to the computation of the neutral curve for a stability

domain for the boundary layer flow under a solitary wave itself.

### C.1 Validation by means of the Blasius boundary layer flow

Opposed to the Orr-Sommerfeld solver, no explicit reference values are given enabling to pin down the correct implementation by means of a concrete number. Therefore, we recalculated two cases given in Bertolotti et al. (1992) to verify the correctness of the present method. These two cases consist in computing the amplification of a Tollmien-Schlichting wave for the frequencies  $F = 50 \cdot 10^{-6}$  and  $F = 220 \cdot 10^{-6}$ , respectively. The results of the present computations can be seen in figures 30 and 31. These can be compared directly to the graphs in figure 4(a) and 4(b) in Bertolotti et al. (1992). Digitizing the amplification curves from this reference we find that the results agree to plotting scale. The amplification curves computed by means of the Orr-Sommerfeld equation are slightly different. However, Bertolotti et al. (1992) did not give any details on the implementation and resolution used for their Orr-Sommerfeld equation solver. The resolution used for the computation of the amplification curves was  $N_{\text{OSE}} = 120$  and  $N_{\text{PSE}} = 120$  for both cases.

### C.2 Validation by means of the boundary layer under a solitary wave

Similar to the verification of the Orr-Sommerfeld solver, we computed the neutral curve for the boundary layer flow under a solitary wave using the present parabolic stability equation solver derived in subsection 3.3 for different resolutions  $N_{\text{PSE}}$ . The case chosen was  $\epsilon = 0.3$  and  $\delta = 4.75 \times 10^{-4}$ . The results can be seen in figure 32. As can be observed the curves for  $N_{\text{PSE}} \geq 140$  are coinciding on a plotting accuracy. The higher the resolution, the better the curves follow this ultimate curve. For all the simulations in section 4, we used a resolution of  $N_{\text{PSE}} = 180$ .

## D Validation of the Navier-Stokes solver

The spectral Legendre-Galerkin solver NEK5000 has been verified and validated over several years. A careful validation of the present case is nevertheless indispensable. As a first test, we validated the present solver by performing a convergence test for the case of no perturbation. A second test is then given by introducing a Tollmien-Schlichting wave and analyzing its amplification for different resolutions.

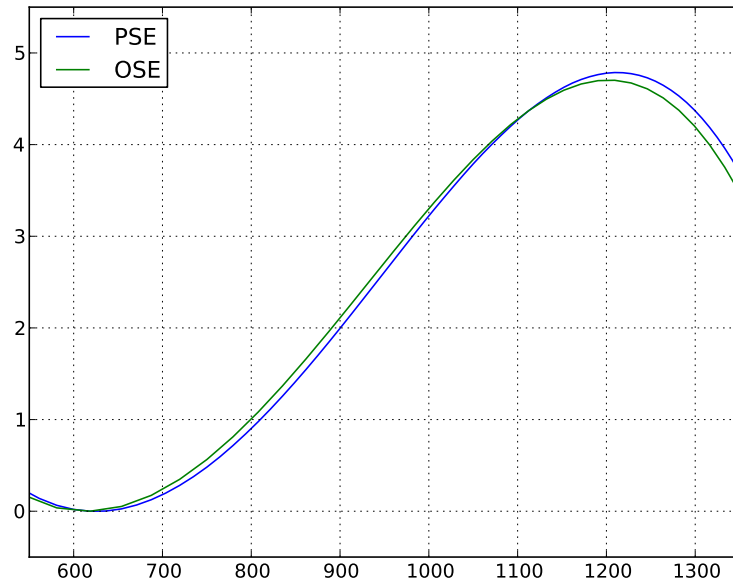


Figure 30: The amplification for a Tollmien-Schlichting wave with frequency  $F = 50 \cdot 10^{-6}$  for the Blasius boundary layer. The graphs were computed by means of the present parabolic stability equation solver (PSE) and the present Orr-Sommerfeld equation solver (OSE). The graphs can be compared to figure 4(b) in Bertolotti et al. (1992).

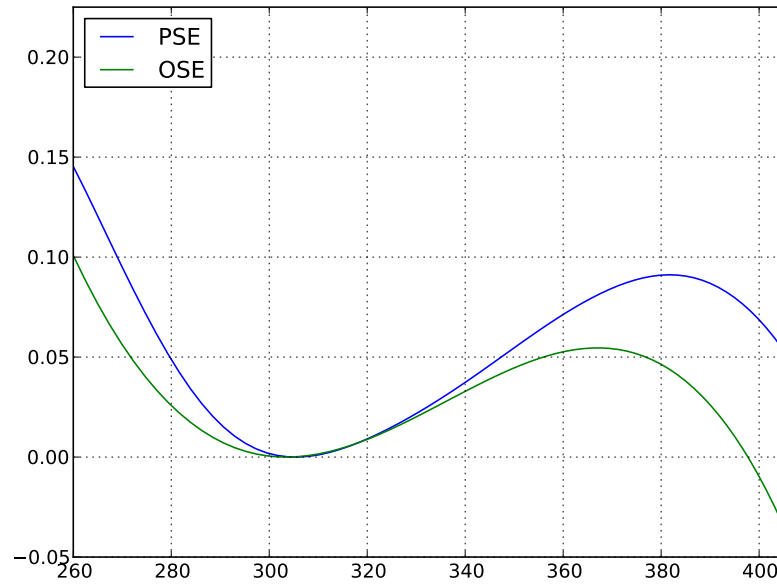


Figure 31: The amplification for a Tollmien-Schlichting wave with frequency  $F = 220 \cdot 10^{-6}$  for the Blasius boundary layer. The graphs were computed by means of the present parabolic stability equation solver (PSE) and the present Orr-Sommerfeld equation solver (OSE). The graphs can be compared to figure 4(a) in Bertolotti et al. (1992).

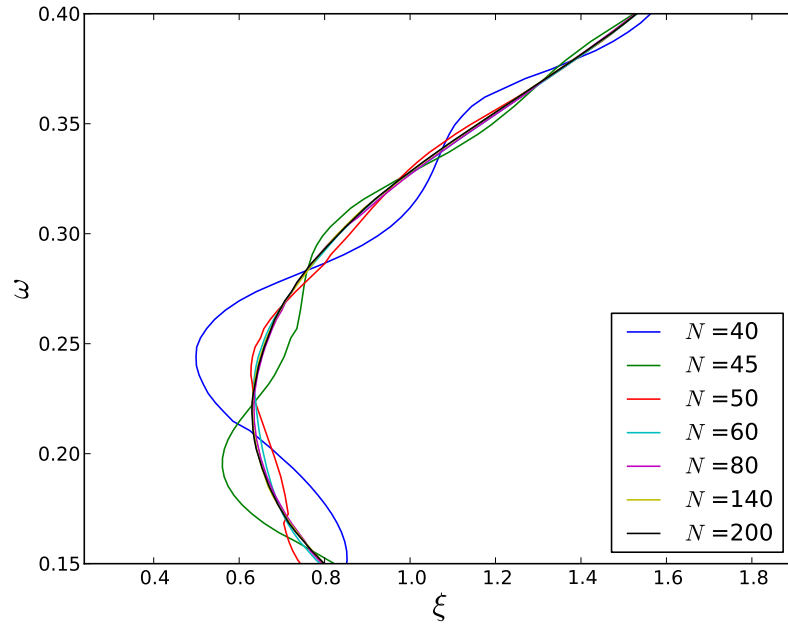


Figure 32: Zoom on the stability curve of figure 15 for  $\delta = 4.75 \times 10^{-4}$  and  $\epsilon = 0.3$ . The curves for different resolutions converge to one single curve for increasing resolution  $N_{\text{PSE}}$ .

## D.1 Validation by means of the boundary layer under a solitary wave

By setting  $u' = 0$ ,  $v' = 0$  in equation (84), the present Navier-Stokes solver should reproduce the solution given by the boundary layer solver. This allowed us to test the convergence properties of the present Navier-Stokes solver. We used the case  $\epsilon = 0.4$ ,  $\delta = 8 \cdot 10^{-4}$ , on a grid given by  $\xi_0 = -0.4$ ,  $\xi_1 = 0.4$  and  $L_y = 41.7$ . The number of elements was chosen relatively low in order to observe some convergence,  $N_x = 20$ ,  $N_y = 1$ . In figure 33, we observe that after a relatively slow convergence up to  $P = 13$ , the solver displays a spectral convergence up to the point, where the error reaches a limit of approximately  $10^{-6}$ , which happens at  $P = 19$ . This saturation is due to the error for the inviscid flow computation being larger than the error by the boundary layer solver and the Navier-Stokes solver. Since it is more efficient to increase the number of elements which can be distributed onto more cores, we chose in general  $P = 11$ ,  $N_x = 300$  and  $N_y = 12$  for the simulations in section 4. As a matter of fact the choice of the velocity  $(U_{\text{base}}, V_{\text{base}})$  at the boundaries of the domain has a huge impact on the accuracy of the boundary layer solution. In figure 34, we plotted different profiles of the horizontal velocity component for the case  $\epsilon = 0.2$  and  $\delta = 4.4 \cdot 10^{-3}$  at the location  $\xi = 9.57$ , which was also investigated in section 4 and by Liu et al. (2007). For all the profiles, we used Grimshaw's solution, equation (6) for the inviscid free stream velocity. As can be seen from figure 34, the linear boundary layer profile computed by means of 95 and the nonlinear boundary layer profile computed by means of the boundary layer solver derived in subsection 3.1 have different courses in the boundary layer, as discussed in section 4. However, their value for  $y \rightarrow \infty$  is identical and corresponds to the value given by Grimshaw's solution at the bottom of the solitary wave. If applying the values for  $(U_{\text{base}}, V_{\text{base}})$  computed using the nonlinear boundary layer solver on the boundary of the domain for the Navier-Stokes solver, we observe that the profiles computed by means of the nonlinear boundary layer solver and the Navier-Stokes solver are identical up to plotting accuracy, cf. figure 34. This is, however, not the case when applying the linear solution, equation (95) together with the correct normal velocity component, equation (97) at the boundaries of the domain for the Navier-Stokes solver. The profile displays in this case a different free stream velocity. Due to the nonlinearity of the Navier-Stokes solver, the linear boundary layer solution on the top boundary could not be satisfied without violating continuity. Therefore, in order to satisfy continuity, additional fluid is pushed in horizontal direction, leading to a different value of the free stream velocity and a second boundary layer at the top of the computational domain.

## D.2 Validation by means of the amplification of a Tollmien-Schlichting wave

The good agreement between amplifications computed by the parabolic stability equation solver and the Navier-Stokes solver in section 4 is by itself a valida-

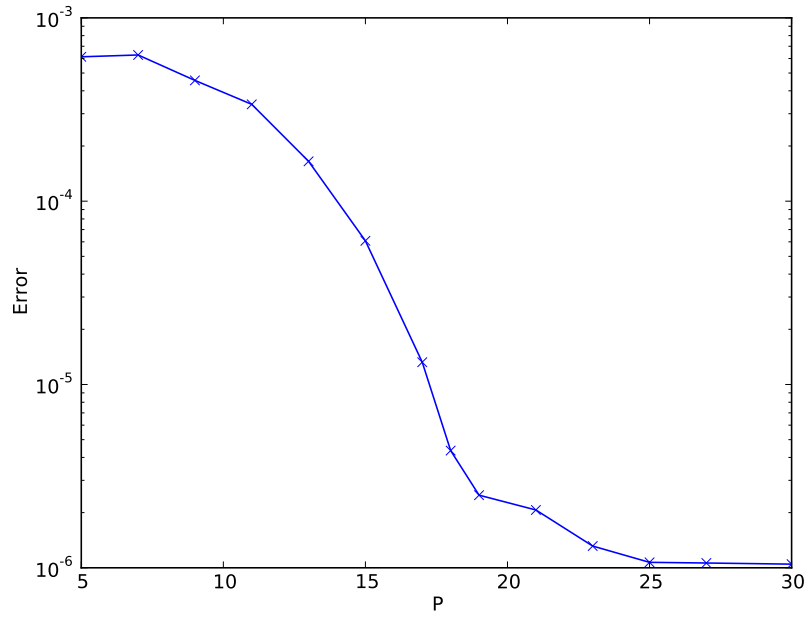


Figure 33: Convergence of the Navier-Stokes solver when increasing the degree  $P$  of the polynomials. The boundary layer was simulated in a domain given by the extensions  $\xi_0 = -0.4$ ,  $\xi_1 = 0.4$  and  $L_y = 41.7$  for the case  $\epsilon = 0.4$ ,  $\delta = 8 \cdot 10^{-4}$ . The number of elements in  $x$  and  $y$  was  $N_x = 20$  and  $N_y = 1$ , respectively. The error was measured in the  $L2$  norm.



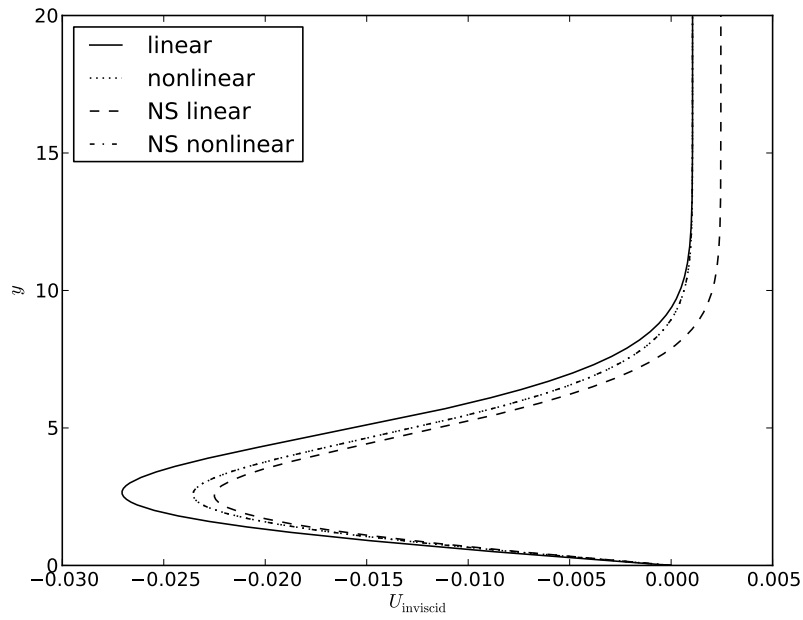


Figure 34: Profiles of the horizontal velocity component for the case  $\epsilon = 0.2$  and  $\delta = 4.4 \cdot 10^{-3}$ . The profiles are computed by means of the linear boundary layer solution (linear), equation (95), the nonlinear boundary layer solution (nonlinear) or by means of the Navier-Stokes solver (NS), using either the linear (NS linear) or nonlinear (NS nonlinear) boundary layer solution at the boundaries of the domain.

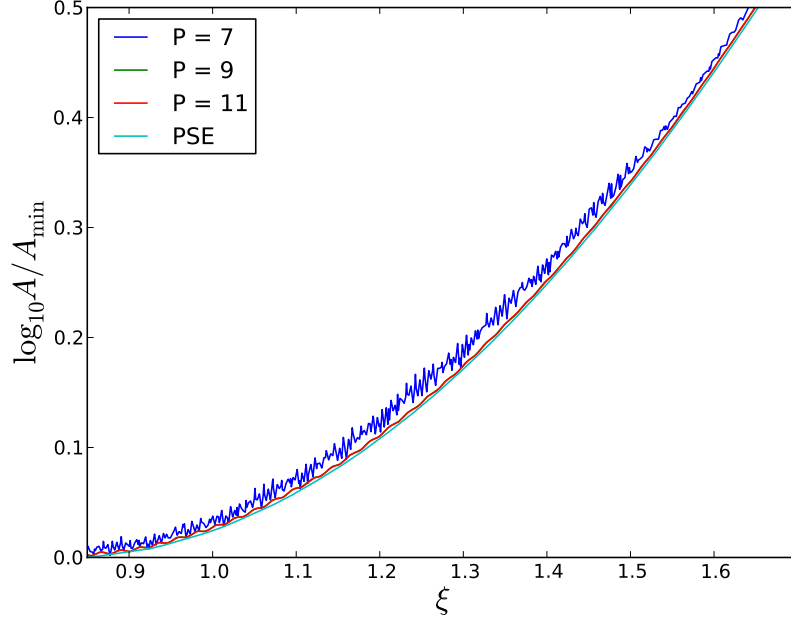


Figure 35: Amplification curves for the case  $\epsilon = 0.4$ ,  $\delta = 8 \cdot 10^{-4}$  and  $\omega = 0.24$  computed by the Navier-Stokes solver for different polynomial degrees  $P$ .

tion for both methods. However, a few words on the numerical issues when computing such amplification curves must be said. In figure 35, we plotted a zoom on the curve in figure 22 using different polynomial degrees  $P$ . As can be observed the curve for  $P = 7$  displays some wiggles. The curves for  $P = 9$  and  $P = 11$  lie on top of each other. However, a closer look reveals that also they display a slight undulation which is not present in the amplification curve by the parabolic stability equation method. The wiggles and the undulation might have their origin in the fact that the Navier-Stokes solver solves the non-linear Navier-Stokes equations whereas the parabolic stability equation method is based on linearized equations. Therefore we might expect a signal with an amplitude of the order of  $10^{-7}$  (corresponding to the omitted nonlinear term in the parabolic stability equation  $\approx (5 \cdot 10^{-4})^2$ ), which is also the amplitude of the undulation in figure 35.

## References

Baines, P. G., Mujumdar, S. J., and Mitsudera, H.: 1996, *Journal of Fluid Mechanics* **312**, 107

- Bertolotti, F., Herbert, T., and Spalart, P.: 1992, *Journal of Fluid Mechanics* **242**, 441
- Blondeaux, P., Pralits, J., and Vittori, G.: 2012, *Journal of Fluid Mechanics* **709**, 396
- Canuto, C., Hussaini, M. Y., Quarteroni, A., and Zang, T. A.: 1993, *Spectral Methods in Fluid Dynamics*, Springer Verlag
- Drazin, P. G. and Reid, W. H.: 1981, *Hydrodynamic Stability*, Cambridge University Press
- Fasel, H.: 1976, *Journal of Fluid Mechanics* **78**, 355
- Fenton, J.: 1972, *Journal of Fluid Mechanics* **53**, 257
- Fischer, P. F., Lottes, J. W., and Kerkemeier, S. G.: 2008, *Nek5000 Web page*, <http://nek5000.mcs.anl.gov>
- Grimshaw, R.: 1971, *Journal of Fluid Mechanics* **46**, 611
- Grosch, C. E. and Orszag, S. A.: 1977, *Journal of Computational Physics* **25**, 273
- Herbert, T.: 1997, *Annual Review of Fluid Mechanics* **29**, 245
- Huerre, P. and Monkewitz, P. A.: 1990, *Annual Review of Fluid Mechanics* **22**, 473
- Jordinson, R.: 1970, *Journal of Fluid Mechanics* **43**, 801
- Joslin, R., Streett, C., and Chang, C.-L.: 1993, *Theoretical and Computational Fluid Dynamics* **4**, 271
- Keller, H. B.: 1978, *Annual Review of Fluid Mechanics* **10**, 417
- Liu, P. L.-F. and Orfila, A.: 2004, *Journal of Fluid Mechanics* **520**, 83
- Liu, P. L.-F., Park, Y. S., and Cowen, E. A.: 2007, *Journal of Fluid Mechanics* **574**, 449
- Miles, J. W.: 1980, *Annual Review of Fluid Mechanics* **12**, 11
- Orszag, S. A.: 1971, *Journal of Fluid Mechanics* **50**, 689
- Osborne, M. R.: 1967, *SIAM Journal on Applied Mathematics* **15**, 539
- Pedersen, G. K., Lindstrøm, E., Bertelsen, A. F., Jensen, A., Laskovski, D., and Sælevik, G.: 2013, *Physics of Fluids* **25**, pp. 23
- Ryhming, I. L.: 2004, *Dynamique des fluides*, Presses polytechniques et universitaires romandes, deuxième édition

- Shuto, N.: 1976, in *Proceedings of 15th Conference on Coastal Engineering*
- Sumer, B. M., Jensen, P. M., Sørensen, L. B., Fredsøe, J., Liu, P. L.-F., and Carstensen, S.: 2010, *Journal of Fluid Mechanics* **646**, 207
- Tanaka, M.: 1986, *Physics of Fluids* **29**, 650
- Trefethen, L. N.: 2000, *Spectral Mehtods in Matlab*, Society for Industrial and Applied Mathematics
- Van Stijn, T. L. and Van De Vooren, A. I.: 1980, *Journal of Engineering Mathematics* **14**, 17
- Vittori, G. and Blondeaux, P.: 2008, *Journal of Fluid Mechanics* **615**, 433
- Vittori, G. and Blondeaux, P.: 2011, *Coastal Engineering* **58**, 206
- White, F.: 2005, *Viscous Fluid Flow*, McGraw-Hill, third edition